Arabian Journal of Chemistry (2023) **16**, 104945

King Saud University

Arabian Journal of Chemistry

www.ksu.edu.sa
www.sciencedirect.com

ORIGINAL ARTICLE

Phosphate and ammonia nitrogen recovery from sewage sludge supernatants by coupled MgO-biomass ash and its potential as heavy metal adsorbent

Zhen Ruan [a], Junzhen Di [a,*], Yanrong Dong [a], Xueying Sun [a], Jianxin Zhang [a], Bofu Yuan [a], Sihang Bao [b]

[a] *College of Civil Engineering, Liaoning Technical University, Fuxin 123000, Liaoning, China*
[b] *College of Mining, Liaoning Technical University, Fuxin 123000, Liaoning, China*

Received 12 December 2022; accepted 23 April 2023
Available online 26 April 2023

KEYWORDS

Biomass ash;
Magnesium oxide;
Phosphate;
Ammonia nitrogen;
Heavy metal;
Resource recovery

Abstract Aiming at the problem of complex treatment for energy solid waste—biomass ash (BA) from thermal power plant and difficult recovery for phosphorus and ammonia nitrogen in sewage sludge supernatants, a coupled MgO-biomass ash (CMBA) was established. CMBA composites were synthesized by in situ thermal-precipitation modification method, which simultaneously achieved recovery of phosphorus and ammonia nitrogen and BA resource utilization, and explored the potential of recovered CMBA (RCMBA) containing phosphate and ammonia nitrogen to remove heavy metal from wastewater. The results showed that magnesium oxide could be effectively loaded on the surface of BA at an $MgCl_2$ concentration of 1.25 M and calcination temperature of 400 °C. pH, adsorbent dosages and initial concentration affected the adsorption capacity of phosphate and ammonia nitrogen by 400CMBA. The existence of K^+, Ca^{2+} and Mg^{2+} ions promoted the removal of phosphate by 400CMBA, but hindered the removal of ammonia nitrogen. The existence of Cl^-, NO_2^- and SO_4^{2-} ions affected the removal of phosphate by 400CMBA. The adsorption processes of 400CMBA for phosphate and ammonia nitrogen can be used with the Langmuir-Freundlich model and the pseudo-second-order model reaching a maximum adsorption capacity of 262.88 mg/g and 122.39 mg/g, respectively. The adsorption behavior was controlled by several processes, spontaneous and thermogenic chemisorption. The saturated adsorbent can be effectively regenerated in 0.1 M HCl solution. After the fifth regeneration, the phosphate and ammonia nitrogen removal rates were less than 50% and 25%, respectively. The adsorption mechanisms of phosphate and ammonia nitrogen by 400CMBA were mainly physical adsorption, electrostatic attraction, ion exchange, complexation reaction and chemical precipitation, among which chemical precipitation was dominated by struvite crystallization was dominant. In addition, RCMBA had a specific removal effect on heavy metal in solutions. Overall, this work provides a feasible way for

* Corresponding author.
E-mail address: dijunzhen@lntu.edu.cn (J. Di).

https://doi.org/10.1016/j.arabjc.2023.104945

the resource utilization of energy solid waste-BA from thermal power plant.

1. Introduction

With further stringent wastewater discharge standards, more and more intensive denitrification and phosphorus removal processes are being applied, resulting in more phosphorus and ammonia nitrogen present in the sewage sludge supernatant (Doyle and Parsons, 2002). However, excess phosphate and ammonia nitrogen in sludge will be rereleased into sewage sludge supernatants again due to hydrolysis in anaerobic sludge digestion treatment. In addition, the supernatant contains high concentrations of organic substances, as well as small amounts of major and minor cations and anions. Excessive discharge of phosphorus and ammonia nitrogen in sewage sludge supernatants will lead to water eutrophication (Dithmer et al., 2015), and causes a decrease in dissolved oxygen levels and cyanobacterial toxin production. What's more, toxic substances released by eutrophication may accumulate through the food chain and threaten human health (Amirbahman and Lake, 2013; Conley et al., 2009; Pei et al., 2015). On the other hand, the reserves of phosphorus in nature are limited. As a non-renewable and indispensable resource, the reserves of phosphorus compounds have been drastically reduced with the further development of agriculture and industry (Bacelo et al., 2020). Facing with the current phosphorus scarcity, it is of great practical importance to develop eco-friendly technologies to prevent eutrophication and simultaneously recover phosphorus and ammonia nitrogen from sewage sludge supernatants.

In recent years, many water pollution control technologies have been developed, including biodegradation, ion exchange, adsorption, and membrane separation (Huo et al., 2012). However, these methods have inherent limitations such as difficult operation, low efficiency, and high energy. Among them, adsorption is a more attractive method, because it has the advantages of high selectivity, easy operation and cost-effectiveness, and has been widely used in industrial wastewater treatment (Bhatnagar et al., 2011). However, high cost, low renewability, and difficulty in disposal after use have hindered the application of conventional adsorbents (e.g., activated carbon, ion exchange resins, zeolites) in developing countries (Lima et al., 2012; Nguyen et al., 2014). In response to these challenges, more and more researchers are focusing on the development of high-performance, low-cost, recyclable, and easy-to-use new adsorbents from agricultural waste, natural minerals and industrial by-products for phosphate and ammonia nitrogen recovery (Fan et al., 2021; Kadirova et al., 2014; Nguyen et al., 2014; Oginni et al., 2020; Xiao et al., 2021).

As a kind of renewable energy generation, biomass power generation has become one of the strategies to solve the energy crisis in some developed and developing countries. As a largely agricultural country, China is very rich in biomass resources. Since the promulgation of the Renewable Energy Law in 2003, biomass power generation technology has developed rapidly (Zhou et al., 2012). In addition, according to the development goals proposed in the 14th Five-Year Plan, it is determined that by 2025, the non-electric utilization scale of geothermal energy heating, biomass heating, biomass fuel, and solar thermal utilization will reach >60 million tons of standard coal. However, in biomass thermochemical conversion to energy production, the problem of biomass ash (BA) production and accumulation is more and more serious, which brings many threats to human health and environmental quality. Recently, it has been reported that BA can be used as a good loading matrix for the adsorption of heavy metal ions or treatment of eutrophic wastewater. BA is a kind of biomass solid product with a porous surface, specific surface area and pore structure (Barbosa et al., 2013; Xu et al., 2016). Using BA to treat wastewater containing nitrogen and phosphorus can achieve the purpose of treating waste with waste. However, the unmodified BA has limited adsorption performance for phosphate and ammonia nitrogen, and is not easy to separate and collect. Therefore, it is necessary to further modify or functionalize BA to improve its adsorption capacity for phosphate and ammonia nitrogen.

Studies have shown that some metals (e.g., magnesium, iron, calcium, and aluminum) contribute to the removal of phosphate and ammonia nitrogen from eutrophication wastewater (Zeng et al., 2020), but there is a disadvantage of high reagent cost and no economic benefit (Liu et al., 2018). Recently, some researchers have pointed out that some metal oxides (e.g., magnesium oxide and calcium oxide) can be used as an economical environmental material, which can be loaded onto the surface of the material through different chemical modification methods to obtain adsorption materials with high adsorption performance (Li et al., 2017). For example, Lv et al., (2022) used calcium modified granular attapulgite to remove phosphate from low phosphorus concentration wastewater. The study showed that when the initial phosphorus concentration was 2.0 mg/L, the adsorption capacity of calcium modified materials to phosphorus increased from 0.074 mg/g to 0.891 mg/g at 298 K and pH 7. Li et al. (2016c) prepared a new type of magnesium oxide impregnated magnetic biochar using sugarcane biochar for phosphate recovery from an aqueous solution. It was found that the adsorption capacity of phosphate was 121.25 mg/g at pH 4. Compared with other metal sources, nano-magnesium oxide modified materials with high reactivity have better performance in the simultaneous removal of phosphate and ammonia nitrogen. Because it can release magnesium to generate struvite crystallization ($MgNH_4PO_4{\cdot}6H_2O$) with phosphate and ammonia nitrogen in water immediately after being added to an aqueous solution. For example, Li et al. (2017) prepared an optimized magnesium oxide impregnated porous biochar for the treatment of swine wastewater. Studies have shown that the maximum adsorption capacity of magnesium oxide biochar is 398 mg/g phosphate and 22 mg/g ammonium. In summary, MgO-modified material is an environmentally friendly, low-cost phosphate and ammonia nitrogen adsorbent. The alkalinity of MgO can neutralize the acid and provide a suitable pH range for the formation of struvite (Park et al., 2021). However, most researchers focus on the single magnesium content or pyrolysis temperature (Li et al., 2017; Zhu et al., 2020), the choice of raw materials (Jiang et al., 2018; Zin and Kim, 2020), and the simultaneous adsorption performance and mechanism of phosphate and/or ammonia nitrogen. Relatively speaking, there are still knowledge gaps in the synergistic effects of magnesium content and pyrolysis temperature on the physical and chemical properties and adsorption capacity of MgO modified materials. In addition, as far as we know, hydroxyapatite containing phosphate ions can form precipitates with high chemical stability with most heavy metal ions in an aqueous solution. Therefore, the adsorption potential of the recovered adsorbent for heavy metal ions was also determined in this study.

At present, the most advanced technology shows that the removal ability of pollutants by adsorption materials obtained by MgO modification with different raw materials is related to the nature of the material itself and the pollutants in the water. There are great differences in the adsorption capacity of different raw materials for different pollutants. In this study, the energy solid waste—biomass ash was used as raw material, and nano-magnesium oxide was loaded on biomass ash through in situ thermal-precipitation modification method to establish a coupled MgO-biomass ash (CMBA). Aiming at the problem of difficult recovery of nitrogen and phosphorus pollutants in sewage sludge supernatants, adsorption materials with better performance were created to achieve its target application. Therefore, this study can

reasonably provide a basis for the influence of the MgO modification process on BA's physical and chemical properties of, and reveal the adsorption performance of CMBA on phosphate and ammonia nitrogen.

The main purpose of this study was: (1) Investigating the removal efficiency of phosphate and ammonia nitrogen under different conditions of an Mg^{2+} addition, calcination temperature and coexisting substances by batch tests, and studying the effect of the pH value, adsorbent dosages, and initial concentration on the adsorption process by response surface methodology (RSM) based on Box-Behnken model. (2) Characterizing the properties of prepared CMBA by scanning electron microscopy energy dispersive spectroscopy (SEM-EDS), X-ray diffraction (XRD) and Fourier transform infrared spectroscopy (FTIR), and revealing the adsorption mechanism of recovered phosphate and ammonia nitrogen through combining adsorption kinetics, isotherm, and thermodynamic models. (3) Investigating the potential of CMBA to treat sewage sludge supernatants by static beaker experiments. (4) Determining the adsorption capacity of recovered CMBA (RCMBA) containing phosphate and ammonia nitrogen for heavy metal in wastewater.

In this study, a coupling MgO-biomass ash system was established, including an understanding of the effect of the MgO modification process on the physical and chemical characteristics of BA, and its performance in removing phosphate and ammonia nitrogen from sewage sludge supernatants. As far as we know, there are few studies on the modification of BA for the treatment of pollutants in water, and there is no research on the loading of nano-magnesium oxide on BA by in situ thermal-precipitation modification method, which further proves the novelty of this work.

2. Materials and methods

2.1. Materials and chemicals

The energy solid waste—biomass ash was used as original material from Fuxin Huinong Biomass Cogeneration Co. All chemicals and reagents were analytical grade without further purification and purchased from Liaoning Quanrui Reagent Co. All solutions were prepared using deionized water. All glassware was soaked in 10% HNO_3 solution for at least 24 h, and then ultrasonic cleaned. After repeated moistening with deionized water, they dried in a constant temperature drying oven for standby. The standard solution containing phosphate and ammonia nitrogen were prepared from KH_2PO_4 and NH_4Cl. The standard solutions of Cu^{2+}, Zn^{2+}, and Pb^{2+} were prepared from $CuSO_4{\cdot}5H_2O$, $ZnSO_4{\cdot}7H_2O$ and $Pb(NO_3)_2$, respectively. In the experiments, obtained a particular concentration of the synthetic solution by diluting the standard solution, and adjusted the pH value with 0.1 M hydrochloric acid or sodium hydroxide.

2.2. Material preparation

Biomass ash was washed with deionized water, dried at 105 °C, and crushed through 80 mesh sieves as the original material BA. Then it was fed into a muffle furnace at different calcination temperatures (200, 300, 400, 500, 600, 700, 800 °C) for 3 h, and the material obtained was denoted as yBA.

The CMBA preparation process consists of three parts. Firstly, BA fully contacted with an $MgCl_2$ solution. Then, a NaOH solution was added to react to produce $Mg(OH)_2$ loaded BA ($Mg(OH)_2$-BA). Finally, $Mg(OH)_2$-BA was roasted at a high temperatures to convert $Mg(OH)_2$ to MgO. Specifically, prepared different concentrations of an $MgCl_2$ solution (0, 0.25, 0.5, 0.75, 1.0, 1.25, 1.5, 1.75 M for Mg^{2+}) and a NaOH solution, where the concentration ratio of Mg^{2+} to OH^- was set to 1:2. Mixed 10 g of BA with 100 mL of an $MgCl_2$ solution, and obtained the impregnating solution by shaking for 30 min at 25 °C, 180 r/min with an oscillator. Then the solution was aged at room temperature for 24 h, filtered, and repeatedly washed with deionized water. Drying was performed at 105 °C to remove the adsorbed water from the surface layer. Finally, the material obtained in the previous stage was crushed and passed through an 80-mesh sieve, then sent to a muffle furnace and calcined at 400 °C for 3 h to get *x*CMBA, where *x* denotes the concentration of Mg^{2+}. To study the effect of 1.25CMBA on phosphate and ammonia nitrogen adsorption at different calcination temperatures (200, 300, 400, 500, 600, 700, and 800 °C), CMBA prepared at different temperatures was denoted as *y*CMBA, where *y* denotes the calcination temperature (Li et al., 2022a, 2022b).

PA-MDP material was obtained by filtering and washing 400CMBA precipitation containing phosphate and ammonia nitrogen, then drying at 80 °C.

2.3. Characterization

The samples used for characterization were dried under vacuum, sieved through 200 mesh sieves, and then used for analysis. The total magnesium addition was measured by an inductively coupled plasma-atomic emission spectrometry (ICP-OES, Varian 710-ES, USA). Before the analysis, the material was degassed at 200 °C in an N_2 atmosphere for 4 h, and then N_2 adsorption/desorption isotherm analysis (micromeritics ASAP2020, USA) was performed to evaluate the BET surface area (S_{BET}), total pore volume (V_{tot}) and pore size distribution of the material. The microscopic features and morphology were characterized using scanning electron microscopy (SEM, FEI-Inspect F50, USA) and energy dispersive X-ray (EDS) spectroscopy. An X-ray diffractometer (XRD, Rigaku-Smartlab9, Japan) was used to determine any phases and structures in the samples. The experimental data were compared with the Joint Committee on Powder Diffraction Standards (JCPDSs) database and analyzed using MDI jade software. In addition, the functional groups were also characterized using Fourier transform infrared spectroscopy (FTIR, Thermo Fisher-Nicolet iS5, USA) at room temperature using KBr particles in the wave number range from 400 cm^{-1} to 4000 cm^{-1}. The zeta potential of BA and CMBA was determined using a pH meter (OHAUS ST3100) at neutral pH.

2.4. Batch adsorption and regeneration tests

The removal of phosphate and ammonia nitrogen was carried out in batch experiments in 150 mL conical flasks at 25 °C and 180 r/min at thermostatic shakers. The removal of phosphate and ammonia nitrogen by *x*CMBA and *y*CMBA was investigated in the same conditions. After 4 h, samples were taken by pipette gun and filtered through a 0.45 μm microporous membrane to measure phosphate and ammonia nitrogen concentrations. The concentrations of phosphate and ammonia nitrogen in the supernatant were determined on a UV–visible spectrophotometer (MAPADA V-1600PC, China) at 700 nm and 420 nm by the ammonium molybdate spectrophotometric

method (GB11893-89) and Nessler's reagent colorimetric method (HJ 535–2009), respectively. The removal efficiency and adsorption were calculated by Eqs. (1) and (2) when the reaction was equilibrated (Di et al., 2022).

$$R_E = \frac{C_0 - C_t}{C_0} \times 100\% \quad (1)$$

$$q_e = \frac{(C_0 - C_e)V}{M} \quad (2)$$

where R_E is the removal efficiency (%), C_0 is the initial mass concentration (mg/L), C_t is the mass concentration of adsorbate in the solution at time t (mg/L), q_e is the adsorption amount at equilibrium (mg/g), C_e is the mass concentration of adsorbate in the solution at equilibrium (mg/L), V is the volume of solution (L), and M is the mass of CMBA (g).

By comparison, the best CMBA preparation conditions (Mg^{2+} addition, calcination temperature) were selected for the subsequent experiments. Subsequently, the main parameters of adsorption (e.g., pH, adsorbent dosage, initial concentration of nutrients, coexisting ions, reaction time and temperature) were investigated. The synthetic wastewater was adjusted at different initial pH varying from 2 to 10 by 0.1 M HCl or NaOH, and its effect on the removal of phosphate and ammonia nitrogen by 400CMBA was evaluated. 100 mL synthetic wastewater was added to 150 mL conical flasks at different 400CMBA masses varying from 0.05 mg to 0.09 mg, and the effect of adsorbent mass on adsorption capacity was studied. Adsorption experiments were performed using different initial phosphate and ammonia nitrogen concentrations, ranging from 20 mg/L to 500 mg/L. The effects of coexisting substances on the removal of phosphate and ammonia nitrogen by 400CMBA were investigated by adding coexisting ions (K^+, Ca^{2+}, Mg^{2+}, SO_4^{2-}, Cl^-, NO_2^-) at concentration varying from 1.0 mM to10.0 mM. Based on the single-factor test, the Box-Behnken model was used to design the RSM optimization test. Design-expert 8.0 software was used to fit the experimental data to the empirical model and perform data analysis. A total of 17 experiments were designed to investigate the interactions between three variables, including the effects of pH value (X_1), adsorbent dosages (X_2, g/L) and initial (X_3, mg/L) on phosphate and ammonia nitrogen removal efficiency. The kinetics, isotherms and thermodynamics were studied under the conditions at contact times varying from 0 to 420 min, an initial nutrient concentration varying from 20 mg/L to 500 mg/L and a temperature varying from 20 °C to 45 °C. Finally, the treatment effect of 400CMBA on the sewage sludge supernatants was tested in the optimal experimental conditions. The sewage sludge supernatants were referred to a wastewater treatment plant in Dalian, and the water quality characteristics were manually dispensed as shown in Table S1.

For the regeneration test, 400CMBA containing phosphate and ammonia nitrogen was washed with deionized water to remove any unabsorbed ions and dried overnight in an oven at 50 °C. In a 150 mL conical flask, the dried 400 CMCBA was in contact with 100 mL 0.1 M HCl eluent at 25 °C and 180 r/min in a constant temperature oscillator. After 240 min, the eluent was separated from 400CMBA. The eluent was filtered through a 0.45 μm microporous membrane to measure the concentration of phosphate and ammonia nitrogen. The separated 400CMBA was washed with deionized water to remove the eluent and dried overnight in an oven at 50 °C. The adsorption capacity of the recovered adsorbent was determined again. Five consecutive adsorption–desorption cycles were carried out. All experiments were repeated three times, and the average value was taken as the final measurement.

According to the previous experimental results of the research group, the initial pH value was adjusted to 5. Weighed 0.01 g PA-MDP material at a dosing rate of 0.1 g/L in 100 mL Pb^{2+} (50 mg/L) solution. Weighed 0.02 g PA-MDP material at a dosing rate of 0.2 g/L in 100 mL Zn^{2+} (30 mg/L) and Cu^{2+} (30 mg/L) solution, respectively. Then placed them in a thermostatic shaker at 298.15 K, 180 r/min. After 12 h, samples were taken by pipette gun and filtered through a 0.45 μm microporous membrane to measure metal concentrations. Metal concentrations were measured thorough an atomic absorption spectrometer (AAS) with an air-acetylene flame (Hitachi-Z2000, Japan). The wavelengths used for the analysis of the Pb^{2+}, Zn^{2+}, and Cu^{2+} were 283.3, 213.9, and 324.8 nm, respectively.

2.5. Adsorption kinetics, isotherms, and thermodynamic models

In order to study the removal of phosphate and ammonia nitrogen, the kinetic data were fitted by the pseudo-first-order model, pseudo-second-order model, general-order model and intraparticle diffusion model (IPD model) (Cavalcante et al., 2022). The equations of each model are shown in Eqs. (3)–(6).

$$\ln(q_e - q_t) = \ln q_e - K_1 t \quad (3)$$

$$t/q_t = 1/(K_2 q_e^2) + t/q_e \quad (4)$$

$$q_t = q_e - \frac{q_e}{\left[k_3 \cdot (q_e)^{n-1} \cdot t \cdot (n-1) + 1\right]^{1/(n-1)}} \quad (5)$$

$$q_t = K_4 \cdot t^{1/2} + C \quad (6)$$

where q_e and q_t are the adsorption capacity of adsorbed phosphate or ammonia nitrogen at equilibrium and time t, respectively (mg/g), K_1 is the proposed primary adsorption rate constant, K_2 is the proposed secondary rate constant, K_3 is the general-order rate constant, n is the order of the general-order model (dimensionless), K_4 is the intraparticle diffusion rate constant, and C is the constant involving thickness and boundary layer. The larger the value of C, the greater the contribution of the boundary layer.

The equilibrium data were fitted by the Langmuir model, Freundlich model and Langmuir-Freundlich model (Sips model) (Yu et al., 2021). The equations of each model are shown in Eqs. (7)–(9).

$$\frac{C_e}{q_e} = \frac{C_e}{q_m} + \frac{1}{(K_L q_m)} \quad (7)$$

$$\ln q_e = \ln K_F + \frac{1}{n} \ln C_e \quad (8)$$

$$q_e = \frac{K_S Q_m C_e^m}{1 + K_S C_e^m} \quad (9)$$

where q_m is the maximum adsorption amount (mg/g), C_e is the concentration of phosphate or ammonia nitrogen in solution at equilibrium (mg/L), K_L is the Langmuir adsorption constant (L/mg), K_F is the Freundlich affinity coefficient ($mg^{(1-n)}L^n/g$), n (dimensionless) is the Freundlich linear constant, K_S is the Sips adsorption constant (L^m/mg^m), and m is the Sips constant, indicating adsorbent inhomogeneity.

The fitness of kinetic and equilibrium data was evaluated by a nonlinear method. Firstly, the Simplex method was used to evaluate the fitness, and then the Levenberg-Marquardt algorithm was used to evaluate by the fitting tool of Microcal Origin Pro 2021 software (Guy et al., 2022). The residual sum of squares (*RSS*), determination coefficient (R^2), adjusted determination coefficient (R^2_{adj}), and residual standard deviation (*SD*) were used to evaluate the applicability of the kinetic and equilibrium models (Cimirro et al., 2022). The mathematical expressions for *RSS*, R^2, R^2_{adj}, and *SD* are shown in Eqs. (10)–(13).

$$RSS = \sum_i^n \left(q_{i,exp} - q_{i,model}\right)^2 \tag{10}$$

$$R^2 = \left(\frac{\sum_i^n \left(q_{i,exp} - \bar{q}_{i,exp}\right)^2 - \sum_i^n \left(q_{i,exp} - q_{i,model}\right)^2}{\sum_i^n \left(q_{i,exp} - \bar{q}_{i,exp}\right)^2}\right) \tag{11}$$

$$R^2_{adj} = 1 - (1 - R^2) \cdot \left(\frac{n-1}{n-p-1}\right) \tag{12}$$

$$SD = \sqrt{\left(\frac{1}{n-p} \cdot \sum_i^n \left(q_{i,exp} - q_{i,model}\right)^2\right)} \tag{13}$$

where $q_{i,model}$ is the individual theoretical q_e value predicted by the model, $q_{i,exp}$ is the individual experimental q_e value; $\bar{q}_{i,exp}$ is the average of all experimental q_e values measured, n is the number of experiments, and p is the number of parameters in the fitting model.

The thermodynamic parameters were determined by the following equations:

$$K = \frac{q_e}{C_e} \tag{14}$$

$$\Delta G = -RT \ln K \tag{15}$$

$$\ln K = \frac{\Delta S}{R} - \frac{\Delta H}{RT} \tag{16}$$

where R is the ideal gas constant (8.314 J/mol·K), T is the Kelvin temperature (K), and K is the thermodynamic equilibrium constant at temperature T. ΔH and ΔS are calculated from the linear plot of $\ln K$ versus $1/K$.

3. Results and discussion

3.1. Effect of Mg^{2+} addition and calcination temperature

The effects of Mg^{2+} addition on phosphate and ammonia nitrogen adsorption are shown in Fig. 1(a). With the increase of Mg^{2+} addition in the solution, the phosphate removal capacity kept increasing, while there was no significant effect on the ammonia nitrogen removal. The correlation data showed a strong dependence of phosphate removal in the solution on Mg^{2+} addition. The adsorption capacity of CMBA on phosphate and ammonia nitrogen was low at low Mg^{2+} addition, probably because of the limited adsorption sites and negatively charged surfaces on the surface of BA. With the addition of Mg^{2+}, the adsorption of phosphate increased significantly. The increase in the equilibrium adsorption of phosphate by CMBA slowed down and reached saturation when the Mg^{2+} addition exceeded 1.25 M (including 1.25 M), and the corresponding removal efficiency was about 98%. The behavior was attributed to the fact that MgO was the primary provider of active centers for phosphate adsorption. The maximum number of MgO particles was reported to depend on the limited external surface area of the carrier (Zhu et al., 2020). Therefore, when the Mg^{2+} addition in the solution increases to a particular value, the amount of MgO loaded on the CMBA surface no longer increases, resulting in the removal of phosphate and ammonia nitrogen remaining almost constant. In fact, the ammonia nitrogen adsorption capacity was little affected by the Mg^{2+} concentration, probably because the ammonia nitrogen adsorption by CMBA was not just controlled by struvite crystallization. Considering the limitation of CMBA adsorption capacity growth due to high Mg^{2+} addition and the related economic factors, 1.25CMBA was selected for further study.

Fig. 1(b) and (c) showed the effect of BA and CMBA on phosphate and ammonia nitrogen adsorption at different calcination temperatures. As shown in Fig. 1(b), the unmodified BA has a particular adsorption capacity for ammonia nitrogen. It may be due to the more abundant functional groups on the surface of BA, which can adsorb ammonia nitrogen by ion exchange. However, BA showed the release of phosphate, and the release of phosphate showed an increasing trend with the increase of calcination temperature. Among them, the highest phosphate release was observed for 800BA with 5.40 mg/g. It may be attributed to the high phosphate content in BA. Comparing the adsorbent materials adsorption capacities for phosphate and ammonia nitrogen before and after modification, the CMBA adsorption capacity for phosphate and ammonia nitrogen is much larger than that of BA. The adsorption capacity of CMBA for phosphate at different calcination temperatures was 600CMBA > 400CMBA > 500CMBA > 700CMBA > 800CMBA > 300CMBA > 200CMBA > $Mg(OH)_2$-BA in order. Unlike phosphate, the CMBA adsorption capacity for ammonia nitrogen at different calcination temperatures was in the order of 400CMBA > 600CMBA > 700CMBA > 500CMBA > 300CMBA > 800CMBA > 200CMBA > $Mg(OH)_2$-BA. CMBA had a strong adsorption capacity for phosphate and ammonia nitrogen when the calcination temperature was more significant than 400 °C, which may be due to the dehydration of the surface-loaded magnesium hydroxide on BA to produce magnesium oxide when the temperature reached 350 °C (Liu et al., 2010). It has been shown that the adsorbent surface activity gradually decreases with the increase of calcination temperature, and the higher temperature is not conducive to the formation of specific surface area and pore structure (Fan et al., 2019; He et al., 2022). Therefore, the CMBA adsorption capacity for phosphate and ammonia nitrogen decreased when the calcination temperature exceeded 600 °C. In conclusion, CMBA can be used as an effective adsorbent for phosphate and ammonia nitrogen

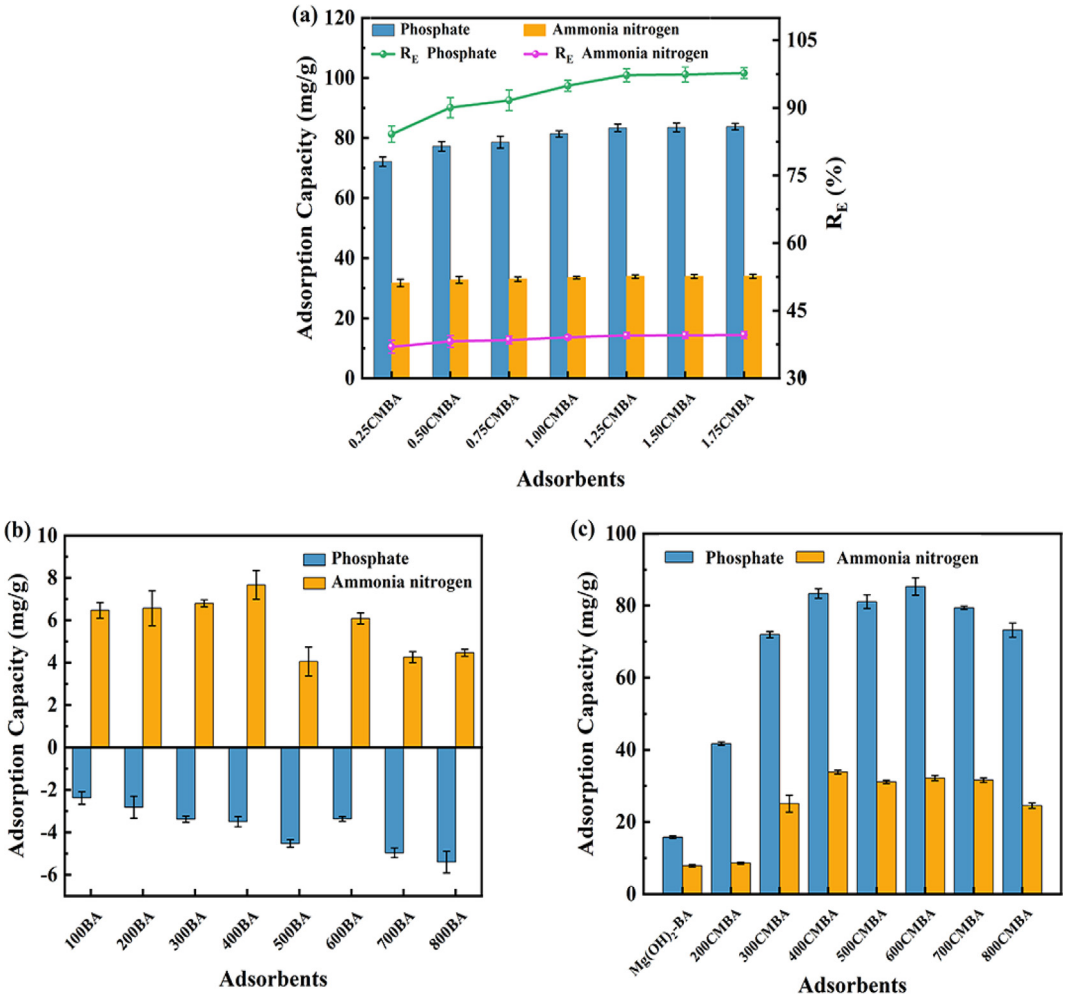

Fig. 1 (a) Effect of Mg^{2+} content on the adsorption of phosphate and ammonia nitrogen onto the CMBA. (b) Effect of pyrolysis temperature on the adsorption of phosphate and ammonia nitrogen onto BA. (c) Effect of pyrolysis temperature on the adsorption of phosphate and ammonia nitrogen onto CMBA. Condition: Initial pH of 7.0, 0.7 g/L adsorbent dosage, 25 °C.

Table 1 Effect of Mg^{2+} additions on the physical and chemical properties of CMBA.

Mg addition amount (M)	Mg^{2+} content (mg/g)	S_{BET} (m^2/g)	V_{tot} (cm^3/g)	*AVP* (nm)
0	4.44	65.12	0.14	8.79
0.25	126.09	50.18	0.25	20.29
0.50	132.66	55.89	0.20	14.06
0.75	141.33	64.10	0.28	17.47
1.00	148.06	66.17	0.26	15.84
1.25	154.58	73.96	0.27	14.87
1.50	161.09	66.76	0.25	15.10
1.75	165.83	59.79	0.20	13.35

recovery. In the subsequent experiments, 400CMBA with good adsorption performance on phosphate and ammonia nitrogen was selected as the adsorbent.

3.1.1. Microstructural characterization of CMBA

As shown in Table 1, BA had a specific surface area of 65.12 m^2/g, a total pore volume of 0.14 cm^3/g, and an average pore diameter of 8.79 nm. With the increase of Mg^{2+} addition, the specific surface area of CMBA increased from 50.18 to 59.79 m^2/g, the total pore volume increased from 0.14 to 0.20 cm^3/g, and the average pore size increased from 8.79 to 13.35 nm. These results agree with those of He et al. (2022). It may be because the added Mg^{2+} hinders the formation of substances such as tar during calcination, thus promoting the formation of pore structures (Zhu et al., 2020). However, the specific surface area and total pore volume of CMBA gradually increased ($\leq$1.25 M) and then decreased ($>$1.25 M) when the Mg^{2+} addition varying from 0.25 M to 1.75 M. Meanwhile,

the average pore size showed a decreasing trend. These results suggest that larger additions of Mg^{2+} may form excess MgO covering the surface of BA, leading to pore blockage (Xu et al., 2018). In addition, the removal of phosphate and ammonia nitrogen by CMBA remained almost constant when the Mg^{2+} addition varying from 1.25 M to 1.75 M, indicating that the specific surface area and total pore volume had a negligible effect on the removal effect. It was reported that the improvement of adsorption performance and removal of pollutants by heat treatment was not significantly related to the changes in specific surface area and pore volume, and the adsorption performance was mainly related to the surface properties (Lv et al., 2022).

The FTIR spectra of BA and *y*CMBA were shown in Fig. 2 (a). The two peaks at 3423 cm^{-1} and 1446 cm^{-1} were due to the stretching vibrations of hydroxyl groups (Lv et al., 2022; Shirazinezhad et al., 2021). The signals at varying from 2921 to 2985 cm^{-1} was due to the asymmetric stretching vibrations of aliphatic C—H (Li et al., 2017). The peaks at 1003 cm^{-1} and 473 cm^{-1} corresponding to the asymmetric stretching vibrations Si—O—Si and Si—O stretching vibrations, respectively (Li et al., 2019). The signals at varying from 692 to 879 cm^{-1} was related to stretching vibrations of —CH_2— and C═C—H bonds (Li et al., 2017). From FTIR, the types of surface functional groups were reduced after making *y*CMBA compared to BA. However, a new peak appeared near 3693 cm^{-1} for 200CMBA, which can be attributed to the stretching vibration of Mg—OH after modification. With the increase of calcination temperature, the absorption peaks of functional groups such as O—H became weaker or disappeared, indicating that the high temperature was not favorable for forming functional groups on the surface of BA. In addition, a new peak at 436 cm^{-1} appeared when the temperature exceeded 300 °C, which was attributed to the stretching vibration of Mg—O, which overlaps with the SiO_2 diffraction peak at 473 cm^{-1} (Zhu et al., 2020). It confirmed that the magnesium hydroxide loaded on the surface of BA was dehydrated to MgO at the calcination temperature of 400 °C.

3.1.2. Characteristics of BA before and after modification

The XRD spectra of BA, $Mg(OH)_2$-BA and 400CMBA samples were depicted in Fig. 2(b). Multiple characteristic diffraction peaks were observed in BA, of which 20.9°(1 0 0) and 26.6°(1 0 1) are relatively more intense and belong to SiO_2 (JCPDS 01–0649). In addition, four new characteristic diffraction peaks appear at 18.6°(0 0 1), 38.1°(1 0 1), 50.8°(1 0 2) and 58.6°(1 1 0), belonging to $Mg(OH)_2$ (JCPDS 07-0239). After calcination, the characteristic diffraction peaks at 18.6°(0 0 1), 50.8°(1 0 2) and 58.6°(1 1 0) were disappeared, and the characteristic diffraction peaks at 38.1°(1 0 1) was weaken. Mean-

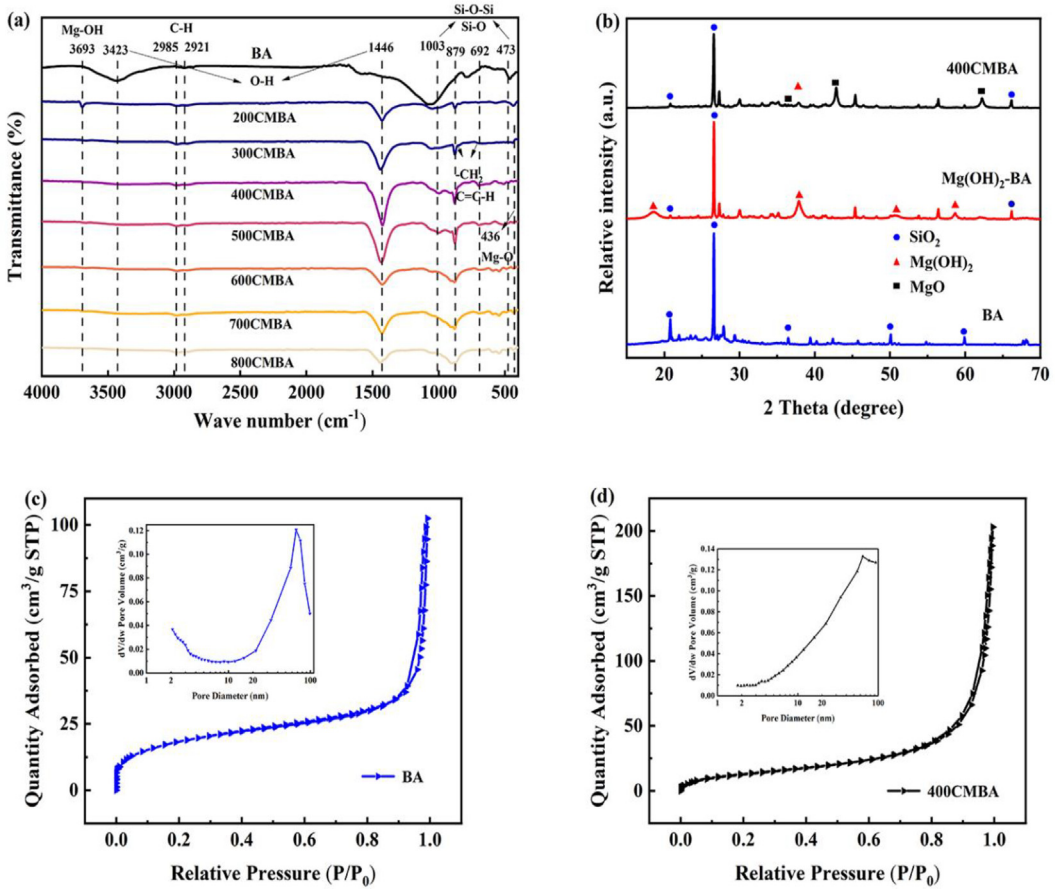

Fig. 2 (a) FTIR spectra of different CMBA. (b) XRD patterns of original biomass ash, $Mg(OH)_2$-BA and 400CMBA. (c) N_2 adsorption/desorption isotherms and the corresponding pore-size distribution (inset) of BA. (d) N_2 adsorption/desorption isotherms and the corresponding pore-size distribution (inset) of 400CMBA.

while, three new characteristic diffraction peaks were observed at 36.9°(111), 42.9°(200) and 62.3°(222), which were confirmed to be MgO (JCPDS 04-0829) diffraction peaks, indicating the conversion of $Mg(OH)_2$ to MgO microcrystals during calcination. Moreover, the relative intensities of the lattice surfaces (100) and (101) in $Mg(OH)_2$-BA and 400CMBA were weaker than those of the unmodified BA due to the coverage of $Mg(OH)_2$ and MgO on the surface of BA.

Fig. 2(c) and (d) showed the N_2 adsorption/desorption isotherms and pore size distributions of BA and 400CMBA. It was observed that the N_2 adsorption isotherms of BA and 400CMBA were consistent with the type IV of the H3 hysteresis loop, which corresponds to the slot holes formed by the accumulation of lamellar particles. As seen from the insets of Fig. 2(c) and (d), the pore size distribution curves were broad, with a predominant number of mesopores and a low number of micropores and macropores for BA and 400CMBA. In addition, the zeta potential of BA was –24.90 mV and the zeta potential of the modified 400CMBA was –8.60 mV. The negative charge on the surface of the modified adsorbent material was reduced, which was beneficial to the phosphate removal from the wastewater.

The surface morphologies of BA and 400CMBA are shown in Fig. 3(a) and (b). By SEM analysis, it observed that the surface morphologies of BA residue and 400CMBA were significantly different. The microstructure of BA residue is rod-like, flaky, and block-like, with a relatively smooth surface. With the massive deposition of MgO particles, the surface pore size of 400CMBA decreased and partially showed a fluffy state. As seen from Fig. 3(b), nano-MgO existed in the form of sheets, which were uniformly loaded on the surface of BA, thus significantly increasing the total pore volume of BA (Xie et al., 2014). The EDS spectra of 400CMBA is shown in Fig. 3(c), and it can be observed that the distribution of element C is uniform. In contrast, the distribution regions of Mg and O are closely related, indicating the generation of nano-MgO. In addition, small peaks of Si, Cl, Ca, and K elements also appeared in the spectrum of Fig. 3(d). Thus, the elemental composition of 400CMBA consists of C (15.47 wt%), Mg (49.43 wt%), O (25.89 wt%), Si (5.40 wt%), Cl (2.28 wt %), Ca (1.05 wt%) and K (0.49 wt%).

3.2. Adsorption research

3.2.1. Effect of pH value

The removal effects of 400CMBA on phosphate and ammonia nitrogen at different pH value are shown in Fig. 4(a). The trends of phosphate and ammonia nitrogen were similar at pH varying from 2 to 10, and the adsorption ability of 400CMBA on them was strongly dependent on the pH value. When the pH value changed from 2 to 3, the adsorption of phosphate and ammonia nitrogen by 400CMBA increased sharply. The equilibrium adsorption amounts of phosphate and ammonia nitrogen increased from 7.00 mg/g and 1.79 mg/g to 56.68 mg/g and 22.81 mg/g, respectively, and continued to increase at a relatively low rate until the pH value reached 7. The best adsorption effect was achieved at this time, with the adsorption amounts of phosphate and ammonia nitrogen peaking at 83.37 mg/g and 33.86 mg/g, respectively. When the pH value was increased, the adsorption capacity decreased at a relatively fast rate, especially for phosphate. And the adsorption amounts of phosphate and ammonia nitrogen decreased to 63.28 mg/g and 13.07 mg/g at pH 10. Considering the removal efficiency and operational feasibility, the initial pH value of 7 was chosen in the following experiments.

Fig. 4(a) also shows the change of solution equilibrium pH value after adsorption of phosphate and ammonia nitrogen at different initial pH value. At an initial pH value of 2, the solution equilibrium pH value was only 2.87, which limited the reaction. This may be because the surface of BA was still negatively charged in an aqueous solution with an initial pH of 2. At the same time, the phosphate in the solution exists in the form of H_3PO_4 and lacked electrostatic adsorption. Therefore, the adsorption capacity of 400CMBA for phosphate was small (Zhu et al., 2020). At an initial pH value varying from 3 to 8, the equilibrium pH of the solution was near 9, and the MgO on the surface of BA underwent a strong protonation reaction $\equiv MgO + H_2O \rightarrow \equiv MgOH^+ + OH^-$ (Li et al., 2016c). It shows that 400CMBA can maintain a higher equilibrium pH under lower initial pH conditions. This indicates that 400CMBA has alkalinity self-sufficiency and can adsorb phosphate and ammonia nitrogen in a wide initial pH range (Li et al., 2022a, 2022b). With the increase of the initial pH value from 3 to 10, H_3PO_4 was gradually deprotonated to HPO_4^{2-} and $H_2PO_4^-$. At this time, the positively charged 400CMBA on the surface would show a strong affinity for the negatively charged phosphate, leading to an increase in the adsorption capacity of 400CMBA on phosphate (Li et al., 2016b). However, due to the increasing pH value, the increasing concentration of OH^- and phosphate produced a violent competition for adsorption sites on the positively charged adsorbent surface, and the electrostatic adsorption between phosphate and adsorbent weakened, eventually leading to a decrease in phosphate adsorption (Xiong et al., 2017). Although the positively charged surface of 400CMBA may not be favorable for the adsorption of positively charged ammonia nitrogen considering electrostatic adsorption, the best adsorption capacity of ammonia nitrogen was achieved at pH 7. It might indicate that the adsorption of ammonia nitrogen was controlled by different processes (Li et al., 2017). Furthermore, the adsorption capacity of 400CMBA for ammonia nitrogen decreases when pH > 8, which may be due to the loss of ammonia nitrogen as NH_3 gas under strongly alkaline conditions (Li et al., 2022a, 2022b). In summary, the adsorption of phosphate by 400CMBA was mainly through electrostatic adsorption, and the adsorption of ammonia nitrogen was affected by a combination of effects. 400CMBA showed strong adsorption capacity at a wide initial pH value varying from 5 to 9, which was favorable for applying 400CMBA in sewage sludge supernatants.

3.2.2. Effect of adsorbent dosages

Investigated the effect of 400CMBA dosages on the phosphate and ammonia nitrogen adsorption, and the results are shown in Fig. 4(b). 400CMBA dosages showed a proportional decrease in adsorption capacity with increasing dosages from 0.5 to 0.9 g/L. In contrast, the equilibrium removal efficiency of phosphate and ammonia nitrogen showed a significant increasing trend. At the dosage of 0.7 g/L, the removal efficiency of phosphate and ammonia nitrogen reached 97.26% and 39.50%, respectively. It may be attributed to the increase

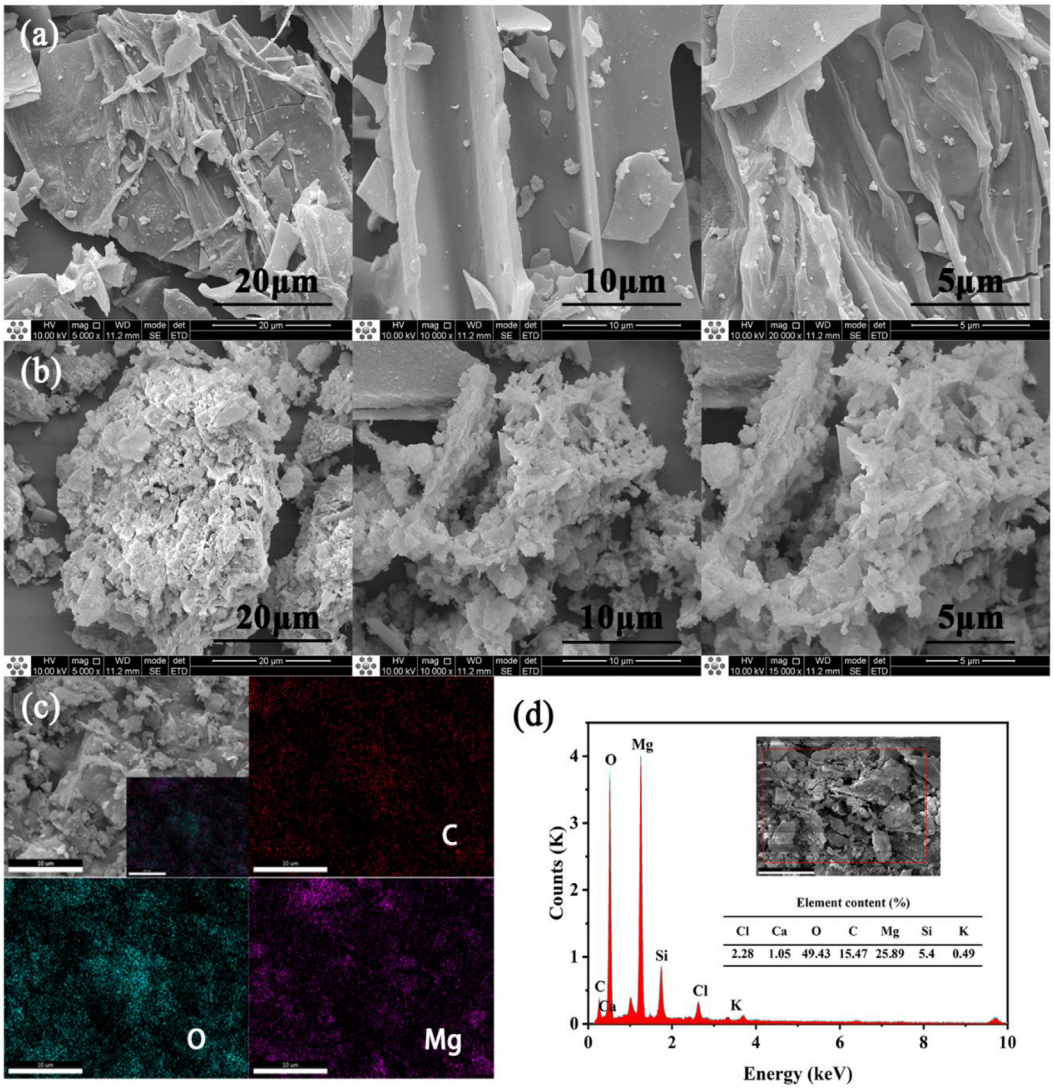

Fig. 3 (a) SEM images of BA. (b) SEM images of 400CMBA. (c) The selected area of 400CMBA for EDS analysis. (d) Elements content of the selected area in EDS analysis.

in the dosage resulting in 400CMBA providing more adsorption sites and a larger surface area, thus favoring the removal of more phosphate and ammonia nitrogen (Edet and Ifelebuegu, 2020). The decrease in adsorption capacity was attributed to the splitting effect of the concentration gradient between the adsorbent and the adsorbate (Albadarin et al., 2012). However, when the dosage exceeded 0.7 g/L, the reaction tended to equilibrium and the removal efficiency of both did not increase significantly. Therefore, the optimal adsorbent dosage was 0.7 g/L, considering the adsorption effect and economic cost.

3.2.3. Effect of initial concentration

The equilibrium adsorption capacity of 400CMBA for phosphate and ammonia nitrogen at different temperatures with the initial concentrations are shown in Fig. 4(c) and (d). The equilibrium adsorption capacity of 400CMBA increased with the initial concentration of phosphate and ammonia nitrogen, and then gradually reached the equilibrium. The increase may be due to the rise in the concentration of phosphate and ammonia nitrogen, which increases the collision with the adsorption sites. Also, the concentration gradient of phosphate or ammonia nitrogen between the solid and liquid phases increased mass transfer driving force, which facilitated the reduction of mass transfer resistance to increase the adsorption capacity (Younes et al., 2020). However, the removal of phosphate and ammonia nitrogen by 400CMBA increased and then decreased with increasing initial concentrations, reaching the maximum removal efficiency when the initial concentrations of phosphate and ammonia nitrogen were near 60 mg/L. It suggested that the adsorption of phosphate and ammonia nitrogen by 400CMBA may be more suitable for higher concentrations of sewage sludge supernatants. The adsorption capacity of 400CMBA decreased when the temperature increased from 298.15 to 318.15 K, indicating that the increase in temperature was not favorable for the removal of phosphate and ammonia nitrogen by 400CMBA.

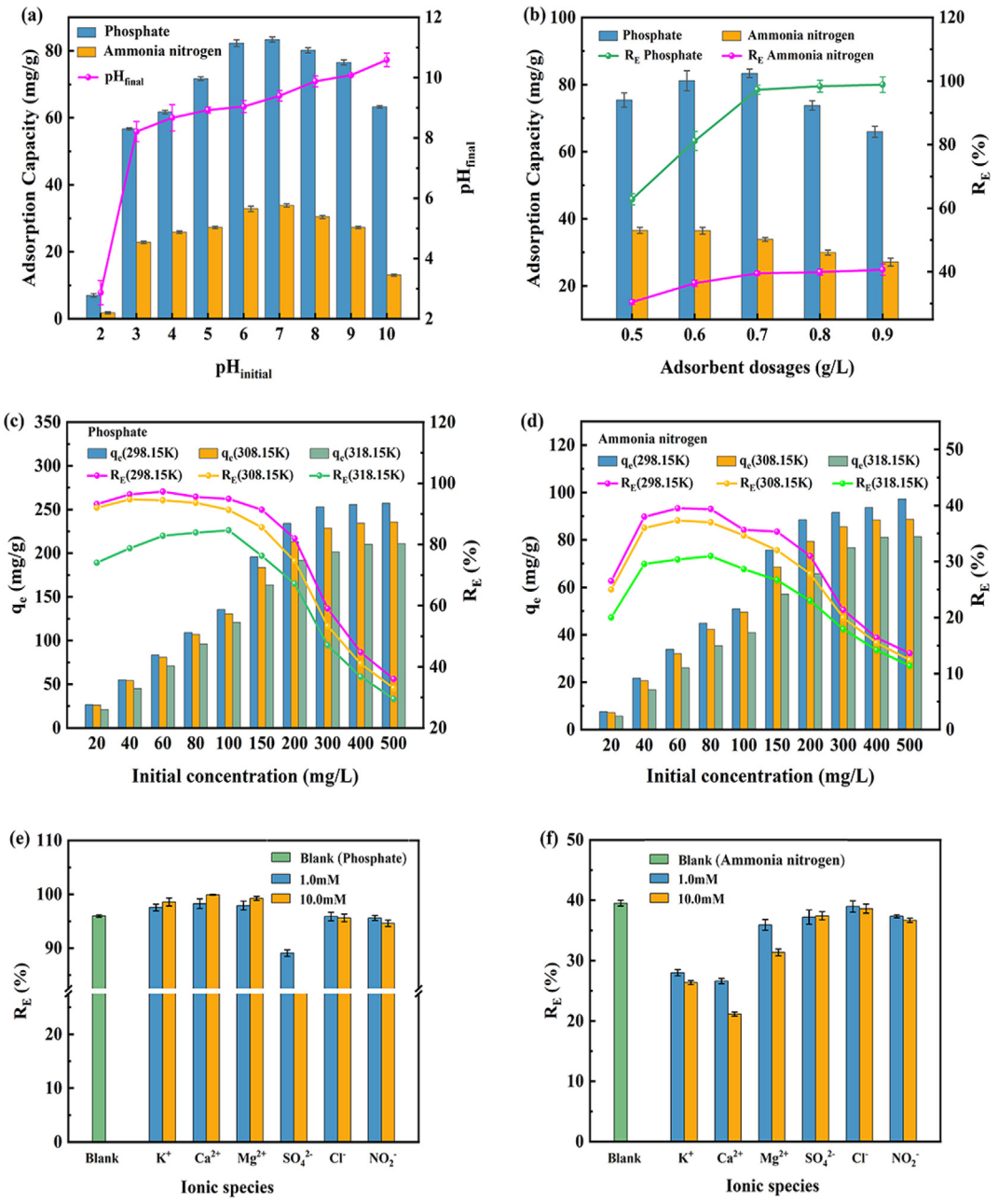

Fig. 4 Effect of $pH_{initial}$ value (a), adsorbent dosages (b), initial concentration (c,d), and coexisting ions (e,f) on the adsorption of phosphate and ammonia nitrogen removal.

3.2.4. Effect of coexisting ions

The results of the effect of single coexisting substances on the removal of phosphate or ammonia nitrogen by 400CMBA are shown in Fig. 4(e) and (f). From Fig. 4(e) and (f), the cations (K^+, Ca^{2+}, Mg^{2+}) had a facilitating effect on the removal of phosphate. When the concentration of cations was increased from 0 to 10 mM, the removal of phosphate risen from 97.26% to 98.55%, 99.9% and 99.23%, respectively. It had been reported that the presence of K^+ in the solution competes with ammonia nitrogen to form K-struvite (Huang et al., 2019), resulting in a slight increase in phosphate removal efficiency. When Ca^{2+} was alone in the solution, it immediately reacted with phosphate to form amorphous calcium phosphate and prevents the formation of struvite crystallization (Li et al., 2020). Mg^{2+} played an essential role in the process of struvite crystallization. The large amount of Mg^{2+} may lead to the conversion of struvite crystallization into magnesium phosphate and promote phosphate removal (Xie et al., 2021). In the presence of Cl^-, the phosphate removal efficiency of 400CMBA had little change, indicating that the effect of Cl^- on the phosphate adsorption process can be ignored. It is well known that the anions adsorbed on the adsorbent via outer sphere complexes are strongly influenced by the ionic strength and coexisting anions, and these coexisting anions can also form outer sphere complexes by electrostatic forces. In contrast, the anions adsorbed on the adsorbent via inner sphere complexes

have low sensitivity to ionic strength and coexisting anions (Du et al., 2017). Apparently, inner sphere complexes were involved in the phosphate adsorption process on 400CMBA, while Cl^- was weakly bound to the surface position of metal hydroxides to form outer sphere complexes, which leads to ineffective competition for Cl^- (Li et al., 2016a; Lu et al., 2014). When NO_2^- was present, the phosphate removal efficiency decreased slightly. It has been reported that elements in the same main group have similar chemical properties and molecular structures (Zhang et al., 2013). When they were present together, intense competition occurs on the surface of the adsorbent. Clearly, the results of this study were not consistent with this conclusion. In addition, when SO_4^{2-} was present, the phosphate removal efficiency of 400CMBA significantly decreased with the concentration of SO_4^{2-}. It may be due to the strong competition of SO_4^{2-} for adsorption sites on the adsorbent surface. Chemically, the ionic radius of SO_4^{2-} (0.230 nm) is larger than that of Cl^- and NO_2^- (both less than 0.200 nm) and like that of $H_2PO_4^-$ (0.238 nm). Therefore, the presence of SO_4^{2-} competed for positive charge sites on the adsorbent surface and reduced phosphate removal (Li et al., 2016a; Li et al., 2017). Overall, the results indicated that in the coexistence of Cl^-, NO_2^- and SO_4^{2-} presence, the phosphate removal efficiency decreased according to $Cl^- > NO_2^- > SO_4^{2-}$.

As seen in Fig. 4(f), the presence of cations had a negative effect on the removal of ammonia nitrogen. When the concentration of cations increases from 0 to 10 mM, the removal efficiency of ammonia nitrogen decreased from 39.5% to 26.34%, 21.15% and 31.35%, respectively. The reduction of ammonia nitrogen removal efficiency was mainly due to the formation of K-struvite, amorphous calcium phosphate and magnesium phosphate. In addition, Fig. 4(f) showed that the anions (SO_4^{2-}, Cl^-, NO_2^-) had little effect on the adsorption of ammonia nitrogen, and no significant changes were found.

3.2.5. RSM model

The experimental design of the Box-Behnken model and the predicted and actual values of phosphate and ammonia nitrogen removal are shown in Table S2. A quadratic regression model was used to explore the relationship between the independent variables and the responses, and the following equations were obtained.

$$\begin{aligned} \textit{Phosphate removal rate} = {} & 96.71 - 0.3237X_1 + 7.82X_2 \\ & + 0.9187X_3 - 0.015X_1X_2 \\ & + 0.2275X_1X_3 - 1.66X_2X_3 \\ & - 4.99{X_1}^2 - 8.47{X_2}^2 - 0.9977{X_3}^2 \end{aligned}$$

$$\begin{aligned} \textit{Ammonium removal rate} = {} & 39.22 - 0.2962X_1 + 2.95X_2 \\ & - 0.2225X_3 - 0.0675X_1X_2 \\ & + 0.0950X_1X_3 + 0.3850X_2X_3 \\ & - 2.96{X_1}^2 - 4.17{X_2}^2 - 1.69{X_3}^2 \end{aligned}$$

Analysis of variance (ANOVA) was used to test the model's reliability, and the results are shown in Tables S3 and S4. According to the ANOVA and significance check of the regression models, the F-values of the regression models for phosphate removal and ammonia nitrogen removal were 68.92 and 222.79, respectively, with P-values less than 0.001, indicating that the models reached a significant level and were statistically significant, and could be used to substitute the actual points of the test for the result analysis. The multivariate correlation coefficients R^2 of the two models were 0.9888 and 0.9965, respectively. The corrected coefficients of determination R^2_{adj} of the models were 0.9745 and 0.9920, indicating that the two models explained 97.45% and 99.20% of the variation in response values, respectively, further indicating that the regression models were suitable for analysis, prediction and optimization of phosphate and ammonia nitrogen removal efficiency.

The F-values for pH, adsorbent dosing and initial concentration in the phosphate removal model were 0.55, 321.55 and 4.44, respectively, with P-values of 0.48, <0.0001 and 0.07. It indicated that the effect of adsorbent dosages on phosphate removal reached an extremely significant level, and the significant degree of effect was: adsorbent dosages > initial concentration > pH. The F-values of the three single factors in the ammonia nitrogen removal model were 6.84, 678.85 and 3.86 with P-values of 0.03, <0.0001 and 0.09, respectively. It showed that the effects of pH value and adsorbent dosages on phosphate removal reached a significant level, and the significant degree of effect was: adsorbent dosages > pH value > initial concentration.

To comprehensively consider the effects of three factors, pH, adsorbent dosages, and initial concentration, on the removal of phosphate and ammonia nitrogen by 400CMBA, the graphical analysis was made by Design-Expert software. The three-dimensional response surface plots are shown in Fig. 5. As shown in Tables S3 and S4, the p-values of the interaction between pH value and adsorbent dosages in the phosphate and ammonia nitrogen removal models were 0.98 and 0.69, respectively, which were >0.05, indicating that there was an interaction between the two but not significant. The p-values of the interaction between pH value and initial concentration in the phosphate and ammonia nitrogen removal models were 0.72 and 0.57, respectively, which were >0.05, indicating an interaction between the two but not significant. The p-values of the interaction between pH value and adsorbent dosages in the phosphate and ammonia nitrogen removal models were 0.03 and 0.04, respectively, which were less than 0.05, indicating a significant interaction between them.

The optimization function of Design Expert was used to predict the optimal adsorption conditions for 400CMBA based on ensuring the maximum removal of phosphate and ammonia nitrogen by 400CMBA. The removal efficiency of phosphate and ammonia nitrogen was 98.48% and 39.74%, respectively, at pH 6.96, adsorbent dosages of 0.74 g/L and initial concentration of 60.16 mg/L. Considering the feasibility and economic cost of the experiment, made certain adjustments to the experimental results. The optimal adsorption conditions for 400CMBA were finally determined as follows: pH 7.00, adsorbent dosages 0.70 g/L, and initial concentration 60.00 mg/L.

3.2.6. Adsorption kinetics

Kinetics is often used to elucidate the mechanisms that occur during adsorption processes, such as mass transfer processes and diffusion control (González-Hourcade et al., 2022). There-

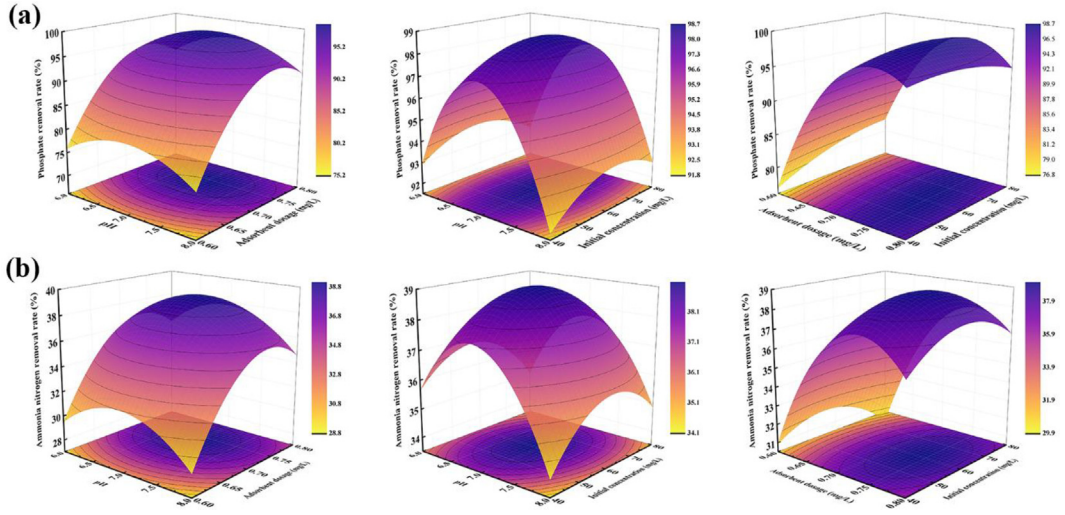

Fig. 5 Interactive effects three variables on the phosphate (a) and ammonia nitrogen (b) removal rate.

fore, the adsorption kinetics of phosphate and ammonia nitrogen by 400CMBA was studied by the pseudo-first-order model, pseudo-second-order model, general-order model and IPD model. In the kinetic experiment, the reaction time reached 420 min when the initial concentration of phosphate and ammonia nitrogen varying from 20 to 100 mg/L. The curves and parameters are shown in Fig. 6 and Table 2, respectively.

In the first 60 min of the reaction, 400CMBA had a faster adsorption rate for phosphate and ammonia nitrogen, and the removal rate of phosphate exceeded 74% and the removal rate of ammonia nitrogen exceeded 23% within 60 min. Subsequently, the removal rate increased relatively slowly, and the removal rates of phosphate and ammonia nitrogen exceeded 96% and 29% at 420 min, respectively. This result was like that reported by Li et al. (2017). The initial rapid adsorption may be due to the electrostatic attraction between the positively charged $MgOH^+$ and the negatively charged phosphate ions (Li et al., 2016a). The subsequent slow growth of the removal rate indicated that the adsorption process may involve intraparticle diffusion (Zhang et al., 2009). In addition, the maximum removal efficiency was achieved when the initial concentration of phosphate and ammonia nitrogen was 60 mg/L, with 97.25% and 39.50%, respectively. Comparing the removal effects at different initial concentrations between 20 mg/L and 100 mg/L, it was observed that at higher concentrations, the removal of phosphate and ammonia nitrogen was better by 400CMBA.

Table 2 shows the kinetic model parameters used to fit the experimental data. The applicability of the kinetic model was evaluated according to R^2_{adj} and *SD*. The higher R^2_{adj} and the lower *SD* indicate that the difference between the experimental and theoretical values of q_e is small (given by the models), so there is an optimal suitable model. Based on these parameters, under the experimental conditions adopted, the R^2_{adj} value of the general-order kinetic model was the highest and the *SD* value was the lowest. Therefore, the general-order model was more suitable for fitting the adsorption process of phosphate and ammonia nitrogen by 400CMBA.

The pseudo-first-order model is an adsorption analysis method based on the solid adsorption capacity proposed by Lagergren. It believes that the mass transfer resistance in the particles limits the adsorption (Sakthivel et al., 2021). The pseudo-second-order model assumes that the adsorption rate is controlled by chemical adsorption, indicating that the adsorption mechanism is the main reason affecting the adsorption (Feng et al., 2018). The general-order model describes the adsorption process in the same order as the chemical reaction (Guy et al., 2022). Therefore, the adsorption process may be chemisorption, and the adsorption rate was influenced by the ligand of the active site on the adsorbent surface and the adsorbate (Di et al., 2022). It likes the results reported by Koh et al. (2019) and Xu et al. (2020a, 2020b) regarding various phosphate adsorbents. In chemical reactions, the reaction order is determined by experiments. With the change in adsorbate concentration, the n (adsorption rate order) values of the general-order kinetic equation were different, and it was difficult to compare the kinetic parameters of the model. Therefore, the adsorption kinetics of phosphate and ammonia nitrogen by 400CMBA were compared with $t_{0.5}$ and $t_{0.95}$. $t_{0.5}$ is the time to reach 50% saturation, and $t_{0.95}$ is the time to reach 95% saturation. $t_{0.5}$ and $t_{0.95}$ were calculated and displayed according to the best fitting model (general-order model).

When the initial concentration was 20 mg/L, the $t_{0.5}$ and $t_{0.95}$ of phosphate were 29.314 min and 112.795 min, respectively, and the $t_{0.5}$ and $t_{0.95}$ of ammonia nitrogen were 25.226 min and 198.076 min, respectively. When the initial concentration was 60 mg/L, the $t_{0.5}$ and $t_{0.95}$ of phosphate were 23.794 min and 123.371 min, respectively, and the $t_{0.5}$ and $t_{0.95}$ of ammonia nitrogen were 37.081 min and 234.321 min, respectively. When the initial concentration was 100 mg/L, the $t_{0.5}$ and $t_{0.95}$ of phosphate were 30.846 min and 153.011 min, respectively, and the $t_{0.5}$ and $t_{0.95}$ of ammonia nitrogen were 28.917 min and 225.552 min, respectively. Observing these values, the adsorption was relatively rapid, and the time for phosphate to reach adsorption equilibrium was faster than that for ammonia nitrogen to reach adsorption equilibrium. In order to ensure that the adsorption process has

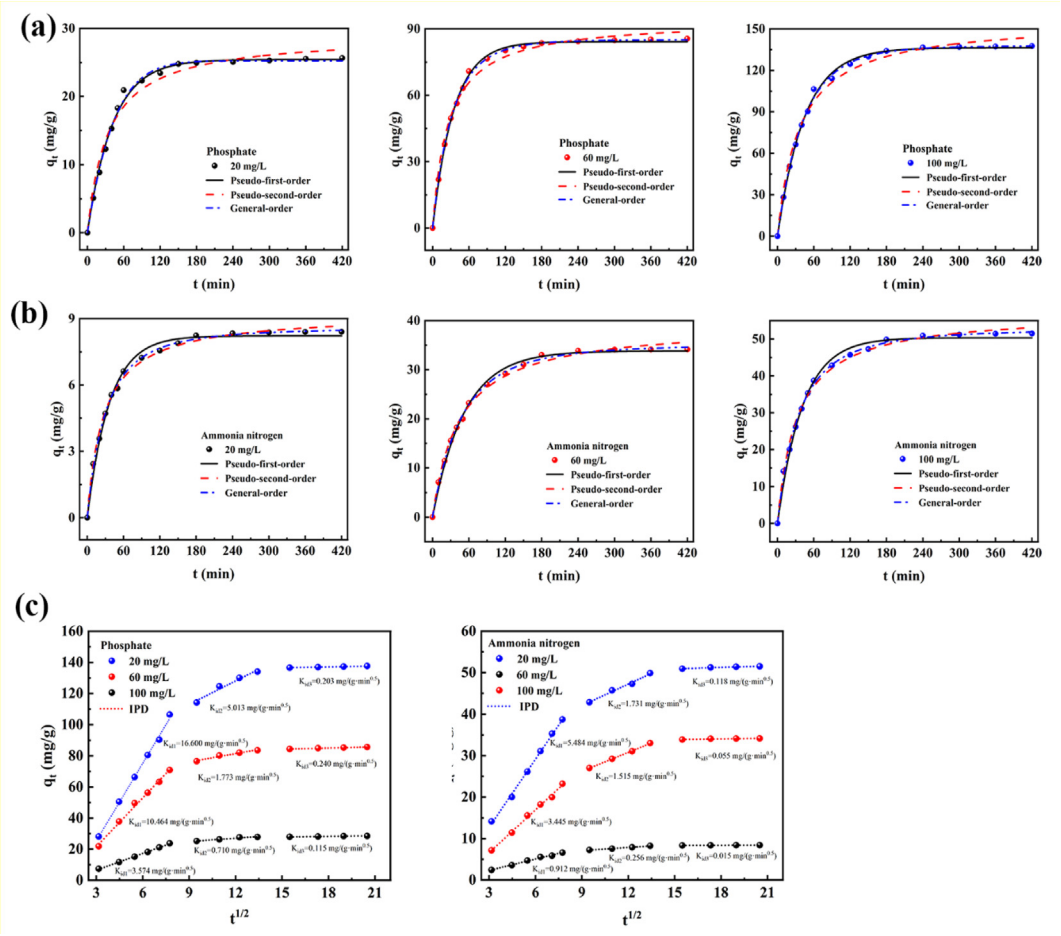

Fig. 6 (a) Adsorption kinetics of phosphate by 400CMBA. (b)Adsorption kinetics of ammonia nitrogen by 400CMBA. (c) Intraparticle diffusion model of phosphate and ammonia nitrogen by 400CMBA. Condition: Initial pH of 7.0, 0.7 g/L adsorbent dosage, 25 °C.

enough time to reach the balance between 400CMBA and nutrients, the established contact time should be slightly higher than $t_{0.95}$. In order to achieve 95% saturation, the equilibrium should be established under the condition that the adsorbent is completely saturated. Therefore, the contact time of 240 min was set for further adsorption isotherm experiments.

For the ion adsorption process from the aqueous phase to the solid phase three mechanisms were generally involved: film diffusion, intraparticle diffusion and active site adsorption. The third step was speedy and was usually neglected. The results are shown in Fig. 6(c). At different initial concentrations, the rate constant K of the adsorption process of phosphate and ammonia nitrogen by 400CMBA decreases according to $K_{id1} > K_{id2} > K_{id3}$, indicating that the adsorption process consists of three parts: rapid adsorption, intraparticle diffusion and equilibrium stage. Comparison of the relevant parameters of the IPD model showed that the fitted results for phosphate and ammonia nitrogen adsorption by 400CMBA were linear but did not pass the origin, indicating that phosphate and ammonia nitrogen adsorption was not only controlled by intraparticle diffusion but also by a combination of mechanisms (Table S5). In addition, the higher R^2_{adj} in the second stage showed that ammonia nitrogen could pass through the pores and voided on the surface of the 400CMBA material and further entered the interior of the material through a combined process of intraparticle diffusion and film diffusion. In summary, the adsorption of phosphate and ammonia nitrogen by 400CMBA was chemisorption controlled by several processes, including internal and external diffusion.

3.2.7. Adsorption isotherms

Adsorption isotherms are useful tools to understand how the interaction between adsorbents and adsorbates occurs (Cavalcante et al., 2022). It can provide reliable information for the possible mechanism and pathway of adsorption. The adsorption process of phosphate and ammonia nitrogen by 400CMBA was further studied by the equilibrium isothermal model. Langmuir, Freundlich and Sips models were used to evaluate the practicability of the equilibrium data of phosphate and ammonia nitrogen for 400CMBA adsorbent. The equilibrium isotherms of phosphate and ammonia nitrogen on 400CMBA at different temperatures (298.15, 308.15, 318.15 K) are shown in Fig. 7, while the three isotherm equilibrium parameters of phosphate and ammonia nitrogen are shown in Table 3.

The Langmuir isotherm model assumes that monolayer adsorption occurs on a uniform adsorbent surface and there is no interaction between adsorbates (Salomón et al., 2020). The Freundlich isotherm model is an empirical equation based

Table 2 Kinetic parameters for adsorption of phosphate and ammonia nitrogen onto 400CMBA.

Model	Phosphate			Ammonia nitrogen		
	Initial concentration (mg/L)					
	20	60	100	20	60	100
Pseudo-first-order						
K_1	2.380×10^{-2}	2.875×10^{-2}	2.240×10^{-2}	2.724×10^{-2}	1.901×10^{-2}	2.418×10^{-2}
q_e (mg/g)	25.42	84.21	136.32	8.22	33.82	50.35
R^2_{adj}	0.9949	0.9889	0.9886	0.9920	0.9945	0.9923
SD (mg/g)	0.598	2.781	4.739	0.229	0.817	1.393
Pseudo-second-order						
K_2	1.010×10^{-3}	4.082×10^{-4}	1.764×10^{-4}	3.930×10^{-3}	5.725×10^{-4}	5.413×10^{-4}
q_e (mg/g)	29.04	94.25	156.28	9.23	39.36	57.17
R^2_{adj}	0.9763	0.9981	0.9975	0.9925	0.9958	0.9952
SD (mg/g)	1.287	1.143	2.242	0.178	0.718	1.104
General order						
K_3	3.194×10^{-2}	1.569×10^{-2}	1.324×10^{-2}	1.213×10^{-2}	7.1×10^{-3}	4.700×10^{-3}
q_e (mg/g)	25.23	85.13	137.74	8.58	35.05	52.79
n	0.896	1.151	1.116	1.456	1.302	1.451
$t_{0.5}$	29.314	23.794	30.846	25.226	37.081	28.917
$t_{0.95}$	112.795	123.371	153.011	198.076	234.321	225.552
R^2_{adj}	0.9950	0.9989	0.9978	0.9978	0.9980	0.9975
SD (mg/g)	0.594	0.884	2.086	0.120	0.489	0.798

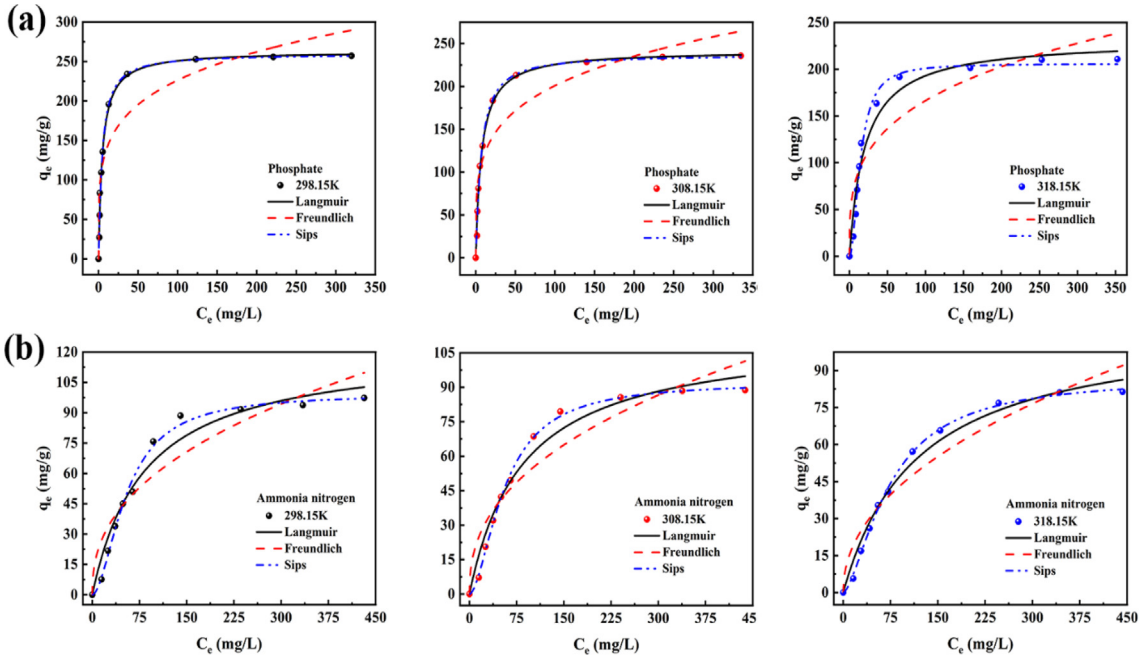

Fig. 7 (a) Isotherms of adsorption of phosphate. (b) Isotherms of adsorption of ammonia nitrogen. Condition: Initial pH of 7.0, 0.7 g/L adsorbent dosage, time of contact of 30 min.

on multilayer adsorption on heterogeneous surfaces (Venkateswarlu et al., 2022). The Sips model is usually used to describe chemical adsorption on heterogeneous surfaces (Zhu et al., 2020). R^2_{adj} and SD values were used to evaluate the applicability of the isotherm model. Based on R^2_{adj} and *SD* values, the Sips model had the highest R^2_{adj} value and the lowest *SD* value under three temperature conditions. This indicates the superiority of the Sips model in describing the adsorption of phosphate and ammonia nitrogen by 400CMBA. It means that the theoretical q_e value of the Sips model is closer to the experimentally found value. Thus, the adsorption of phosphate and ammonia nitrogen on the

Table 3 Adsorption isotherm constants for adsorption of phosphate and ammonia nitrogen onto 400CMBA.

Model	Phosphate			Ammonia nitrogen		
	T (K)					
	298.15	308.15	318.15	298.15	308.15	318.15
Langmuir						
K_L	0.208	0.138	0.050	0.012	0.012	0.008
q_m (mg/g)	262.88	241.87	231.69	122.39	113.12	109.29
R^2_{adj}	0.9904	0.9921	0.9441	0.9475	0.9594	0.9762
SD (mg/g)	6.845	5.552	13.354	5.924	4.756	3.342
Freundlich						
K_F	85.24	70.40	44.63	8.79	8.07	5.16
$1/n$	0.212	0.228	0.286	0.416	0.416	0.473
R^2_{adj}	0.8186	0.879	0.8373	0.8788	0.8903	0.9237
SD (mg/g)	29.821	25.500	26.590	10.495	9.150	6.909
Sips						
K_S	0.1941	0.1213	0.0060	0.0007	0.0009	0.0012
q_m (mg/g)	259.73	237.43	205.86	99.32	92.25	87.49
m	1.075	1.102	1.916	1.802	1.734	1.556
R^2_{adj}	0.9900	0.9926	0.9900	0.9920	0.9969	0.9978
SD (mg/g)	6.539	5.032	5.980	2.446	1.226	0.954

400CMBA surface was a non-homogeneous chemisorption (Yin et al., 2019). The adsorption process was consistent with the Freundlich model at low phosphate and ammonia nitrogen concentrations and with the Langmuir model at high concentrations. It suggested that the adsorption of phosphate and ammonia nitrogen on 400CMBA may be influenced by various mechanisms, including physical and chemical adsorption, which is consistent with the kinetic fit (He et al., 2022).

For the Langmuir model, the maximum adsorption capacities were 259.73, 237.43 and 205.86 mg/g for phosphate and 99.32, 92.25 and 87.49 mg/g for ammonia nitrogen on 400CMBA at temperatures of 298.15, 308.15 and 318.15 K, respectively. Usually $1/n$ represents the adsorption strength, between 0 and 1. The smaller the $1/n$ value, the better the adsorption performance. In this study, the $1/n$ of the Freundlich model is less than 1, which confirms that the adsorption conditions are good, and the smaller $1/n$ value of phosphate indicates that the affinity of 400CMBA to phosphate is stronger than that to ammonia nitrogen (Ahmed et al., 2021).

3.2.8. Adsorption thermodynamics

The adsorption thermodynamics allows further analysis of the influence of adsorption systems and conditions such as adsorbate, adsorbent, and solvent on the adsorption process. Among them, determined the change in Gibbs free energy changes (ΔG), entropy (ΔS) and enthalpy change (ΔH) used to the spontaneity of the adsorption process, the nature of the adsorption process and the applicability of the adsorption process (Edet and Ifelebuegu, 2020). Investigated the effect of thermodynamic temperature on the adsorption properties of 400CMBA on phosphate and ammonia nitrogen by varying the temperature between 293.15 K and 318.15 K. The results are shown in Fig. 8(a), (b) and Table 4. Fig. 8(a) showed that the removal efficiency of both adsorbates showed a trend of increasing and then decreasing with increasing temperature, and reached the best removal effect at the reaction temperature of 298.15 K. When the temperature was low, the number of activated molecules in the reaction system increased with the increase of the reaction temperature, which was favorable to the formation of struvite crystallization. Continuing to increase the reaction temperature, a significant decrease in both phosphate and ammonia nitrogen removal and adsorption capacity occurred, probably because the solubility product of struvite crystallization was inversely proportional to the ambient temperature, which was not favorable for struvite crystallization when the temperature was higher (Hanhoun et al., 2011). Fig. 8(b) demonstrated the Van't Hoff plots for phosphate and ammonia nitrogen at different temperatures. As shown in Table 4, the negative value of ΔG indicated that the adsorption process of phosphate was spontaneous. While the negative ΔG values of ammonia nitrogen gradually tended to positive values, meaning that its adsorption was spontaneous but less efficient at higher temperatures. Negative values of ΔH and ΔS indicated the exothermic nature of phosphate and ammonia nitrogen adsorption and the reduced stoichiometry of the interface between 400CMBA and the solution. The results agreed with the findings of Isik et al. (2021). It had been reported that ΔH values in the range of 2.1 to 20.9 kJ/mol indicate physical adsorption, while ΔH values in the range of 20.9 kJ/mol to 418.4 kJ/mol indicate chemisorption (Yu et al., 2022). In the present study, the ΔH of phosphate was –56.68 kJ/mol, indicating the involvement of chemisorption in the phosphate adsorption process. While ΔH of ammonia nitrogen was –11.27 kJ/mol, indicating that physisorption was involved in the adsorption process of ammonia nitrogen, confirming that the adsorption of ammonia nitrogen by 400CMBA was not only controlled by the formation of struvite crystallization.

3.2.9. Regeneration research

Renewability is an important index to evaluate the performance of adsorbents. The commonly used solvents are NaOH, HCl and alcohols (such as methanol, ethanol). In this study,

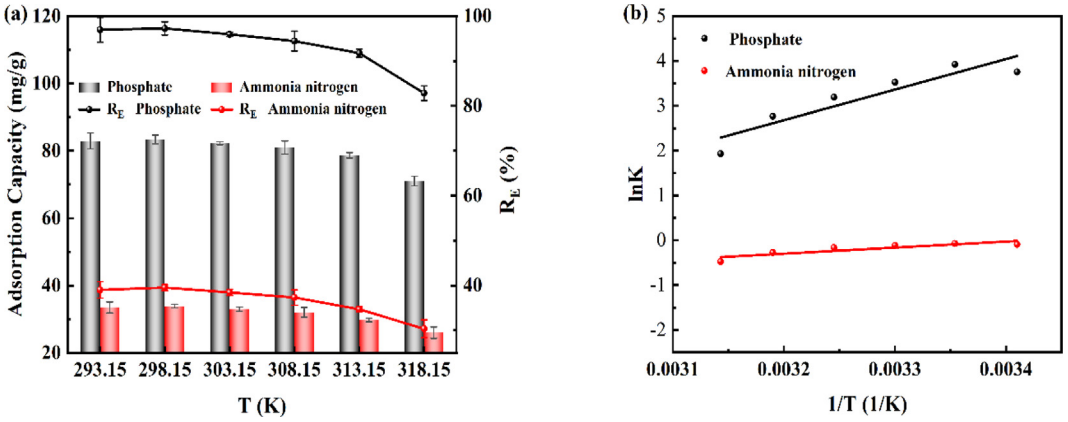

Fig. 8 (a) Effect of temperature on removal capacity. (b) Relationship curve between ln$K$ and $1/T$.

Table 4 Thermodynamic parameters for adsorption of phosphate and ammonia nitrogen onto 400CMBA.

Nutrient elements	ΔH (kJ/mol)	ΔS (J/mol·K)	ΔG (kJ/mol)					
			293.15 K	298.15 K	303.15 K	308.15 K	313.15 K	318.15 K
Phosphate	–56.68	–159.10	–9.16	–9.73	–8.88	–8.17	–7.20	–5.11
Ammonia nitrogen	–11.27	–38.53	0.22	0.17	0.29	0.41	0.72	1.25

0.1 M HCl was used as the desorption solution, and the samples were subjected to 5 adsorption–desorption cycles. The effect of reuse times of 400CMBA on its adsorption capacity is shown in Fig. 9. It can be seen from the figure that the removal ability of 400CMBA to phosphate and ammonia nitrogen showed a large downward trend after 5 cycles, which may be because phosphate and ammonia nitrogen occupied more adsorption sites in the pores of 400CMBA (Li et al., 2021). After the fifth cycle, the removal rates of phosphate and ammonia nitrogen were less than 50% and 25%, respectively. These results indicate that the reusability of 400CMBA is not high. However, to our knowledge, 400CMBA after adsorption of phosphate and ammonia is a potential slow-release fertilizer. The effect of the practical application of recycled 400CMBA in soil on seed growth needs further study.

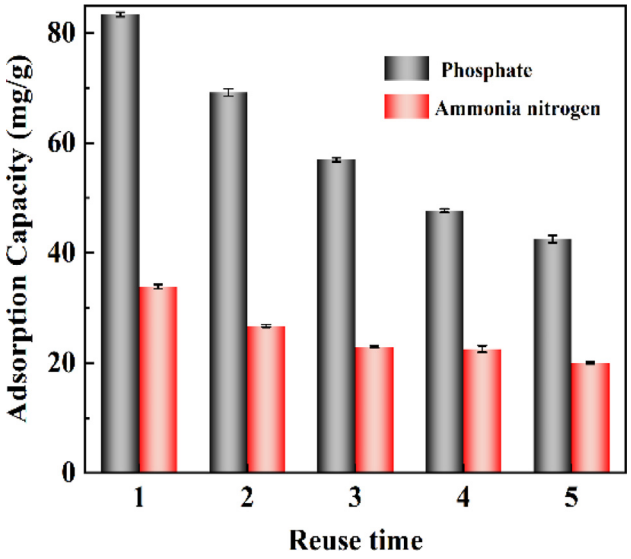

Fig. 9 Effect of reuse times of 400CMBA on removal capacity.

3.3. Adsorption mechanism

Based on the physical and chemical properties of 400CMBA, such as specific surface area, pore size distribution, FTIR and XRD, as well as adsorption data such as initial pH solution, adsorption kinetics, adsorption isotherms and thermodynamic studies, the possible mechanism of phosphate and ammonia nitrogen adsorption on 400CMBA adsorbent can be explained (Fig. 10(a)).

The adsorption of phosphate and ammonia nitrogen from simulated wastewater by 400CMBA can be attributed to five mechanisms: (1) physical adsorption. BA had a large specific surface area and pore structure, and the thermal modification treatment improved the pore structure and increased the adsorption sites to a certain extent, thus improving the physical adsorption performance (Yuan et al., 2020). (2) Electrostatic adsorption. When 400CMBA met the aqueous solution, the MgO on the surface of BA was immediately protonated to the $MgOH^+$ form, which led to an increase of pH value (Zhu et al., 2020). At the pH value range was between 5 and 10, the orthophosphate ions presented in the solution were mainly HPO_4^{2-} and $H_2PO_4^-$ (Li et al., 2022a, 2022b). Therefore, HPO_4^{2-} and $H_2PO_4^-$ were easily adsorbed to the positively charged 400CMBA surface, but were not favorable for the adsorption of positively charged ammonia nitrogen. (3) Ion exchange. BA contains Ca^{2+}, K^+, Mg^{2+} and Na^+ and other cations, which will be ion exchanged with the solution of ammonia nitrogen ions. (4) Complexation reaction. Ligand exchange and complex precipitation are one of the

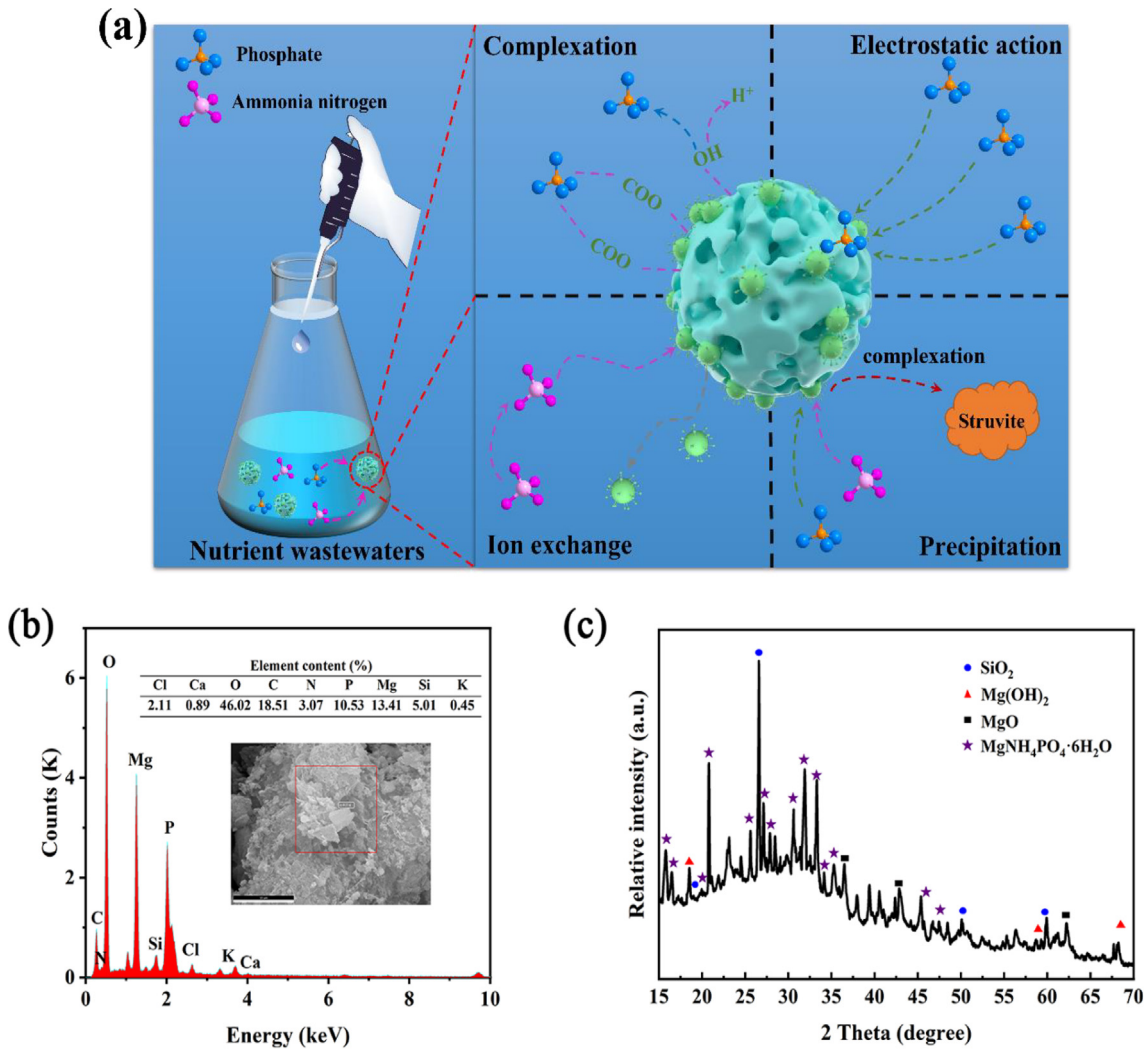

Fig. 10 (a) Proposed adsorption mechanism for uptake of phosphate and ammonia nitrogen onto CMBA. (b) EDX spectra of CMBA after adsorption. (c) XRD patterns of CMBA after adsorption.

adsorption mechanisms for phosphate removal by MgO modified materials (Li et al., 2022a, 2022b). (5) Chemical precipitation. According to previous studies, struvite crystallization was the primary mechanism for removing phosphate and ammonia nitrogen from wastewater (Li et al., 2017). The contact of 400CMBA with the aqueous solution immediately released large amounts of Mg^{2+} and OH^-, which led to an increase of pH value and Mg^{2+} concentration in the aqueous solution, and then Mg^{2+}, phosphate and ammonia nitrogen formed struvite crystallization at the appropriate pH.

To confirm the above mechanism, the precipitates obtained under the optimal reaction conditions were collected, dried, and sieved through a 200-mesh screen, and then characterized by EDS and XRD assays. The EDS spectrum analysis showed that there were phosphorus and nitrogen elements in 400CMBA composites after the treatment of phosphate and ammonia nitrogen wastewater (Fig. 10(b)). The basic components were C (18.51 wt%), Mg (13.41 wt%), O (46.02 wt%), Si (5.01 wt%), Cl (2.11 wt%), Ca (0.89 wt%), K (0.45 wt%), N (3.07 wt%) and P (10.53 wt%). Fig. 10(c) depicted the XRD pattern of 400CMBA after adsorption. XRD analysis showed that after 400CMBA was treated with ammonia nitrogen and phosphorus wastewater, a plurality of diffraction peaks appeared at 15.81°(020), 46.47°(011), 20.85°(111), 21.45°(021), 25.61°(200), 27.09°(130), 30.60°(211), 31.91°(040), 33.28°(022) and 33.67°(211). These diffraction peaks were consistent with the struvite crystallization of $MgNH_4PO_4{\cdot}6H_2O$ (JCPDS 15–0762), which confirmed the formation of struvite crystallization ($MgNH_4PO_4{\cdot}6H_2O$) on the surface of the 400CMBA composite (Cheng et al., 2017). The primary mechanism of fixation of phosphate and ammonia nitrogen in wastewater by the composite material was struvite precipitation. Therefore, 400CMBA in the solution containing phosphate and ammonia nitrogen may undergo the following reactions:

$$MgO + H_2O \rightarrow MgOH^+ + OH^- \tag{17}$$

$$Mg^{2+} + HPO_4^{2-} + NH_4^+ + 6H_2O \rightarrow MgNH_4PO_4 \cdot 6H_2O \downarrow + H^+ \tag{18}$$

$$Mg^{2+} + H_2PO_4^- + NH_4^+ + 6H_2O \rightarrow MgNH_4PO_4 \cdot 6H_2O \downarrow + 2H^+ \quad (19)$$

According to the results of the pH study, the adsorption capacity of phosphate and ammonia nitrogen on 400CMBA adsorbent depends on pH, so electrostatic adsorption is not the main factor for phosphate and ammonia nitrogen removal. In this study, the pH_{final} range was between 9 and 10 (Fig. 4 (a)), which is consistent with the known alkaline environment (pH at around 8–10) for the formation of struvite crystallization. According to the above reaction of struvite crystallization formation, a particular amount of H^+ was released during struvite crystallization to neutralize OH^- generated by MgO hydrolysis. It facilitated the hydrolysis of MgO and the struvite crystallization reaction to the right, thus eliminating the need for an additional base source. In addition, an equal stoichiometric ratio of phosphate and ammonia nitrogen was expected to be removed from the synthetic solution. However, it was found that the amount of phosphate and ammonia nitrogen adsorbed by 400CMBA was not consistent with the ratio of 1:1 M in this study. Still, that phosphate (~0.88 mM) was less than ammonia nitrogen (~1.88 mM) per gram of 400CMBA. The results indicated that the adsorption of ammonia nitrogen by 400CMBA was not only controlled by the formation of struvite crystallization but also by other processes. According to the adsorption kinetic process of ammonia nitrogen and the IPD model data (Table 2), it may be caused by the ion exchange between the positively charged ammonia nitrogen and the internal positively charged cations (Li et al., 2017).

3.4. Effectiveness of 400CMBA treatment of sewage sludge supernatants

Based on the experimental results of the previous synthetic solution, the sewage sludge supernatant adsorption experiments were conducted, and the results are shown in Fig. 11. The adsorption capacity of 400CMBA for phosphate and ammonia nitrogen in the synthetic supernatant was like that of the synthetic solution. In addition to phosphate and ammonia nitrogen, this material also showed some adsorption capacity for COD, which was consistent with the results of Li et al. (2017). The adsorption equilibrium capacities of 400CMBA 86.00 mg/g phosphate, 28.29 mg/g ammonia nitrogen and 257.93 mg/g COD, respectively. In conclusion, the results indicated that 400CMBA had high removal potential for phos-

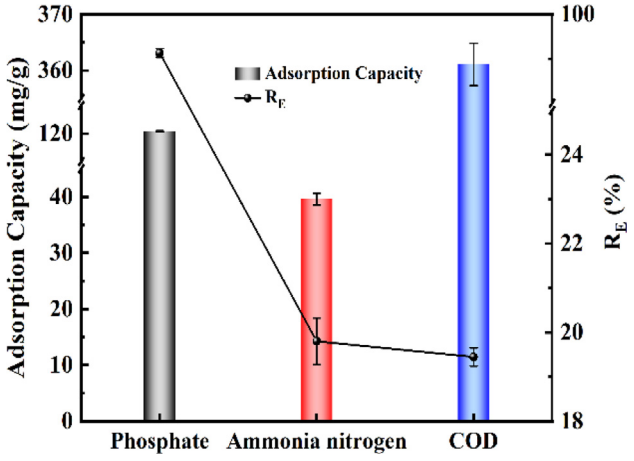

Fig. 11 Potential of 400CMBA on supernatant solutions treatment.

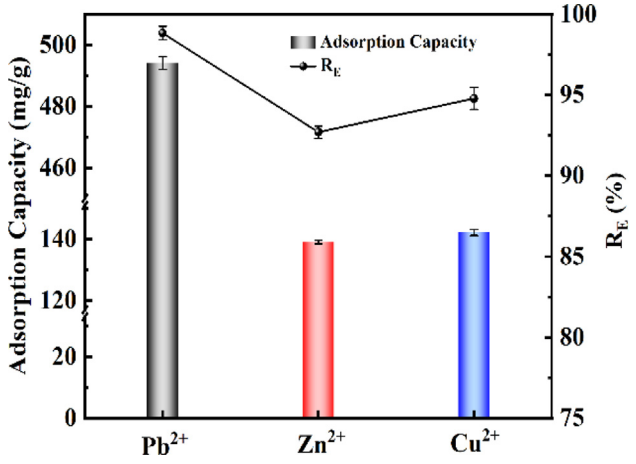

Fig. 12 Potential of RCMBA for heavy metal ions adsorption.

Table 5 Comparison of adsorption capacities of different adsorbents for phosphate and ammonia nitrogen.

Adsorbent	Temperature (K)	q_m (mg/g)		pH	Dosage (g/L)	Equilibrium time (h)	Reference
		Phosphate	Ammonia nitrogen				
Calcium alginate beads	298.15	7.91	15.20	6	5	1	Isik et al., 2021
Iron oxide nanoparticle-zeolite hybrid	303.15	38.91	3.47	6.37	7	0.5	Xu et al., 2020a, 2020b
Calcium alginate-biochar composite	298.15	31.80	12.27	8	4	24	Feng, et al., 2021
Modified clinoptilolite	298.15	0.87	3.33	8.5	110	0.67	Huo et al., 2012
Iron-loaded aminated polyacrylonitrile fiber	298.15	24.14	n.g.	6	0.5	0.08	Xu et al., 2020a, 2020b
Ca-bentonite	293.15	n.g.	46.90	7	5	1.5	Sun et al., 2015
400CMBA	298.15	262.88	122.39	7	0.7	4	This work
	308.15	241.87	113.12				
	318.15	231.59	109.29				

n.g: Not given.

phate, ammonia nitrogen, and dissolved organic matter in the sewage sludge supernatant. The maximum monolayer adsorption capacities of different modified adsorbents for phosphate and ammonia nitrogen are shown in Table 5. The maximum monolayer adsorption capacities of 400CMBA for phosphate and ammonia nitrogen were 262.88 mg/g and 122.39 mg/g, respectively. The 400CMBA composite had obvious advantages in phosphate and ammonia nitrogen removal. In addition to treating sewage sludge supernatants, it can also recover phosphate and ammonia nitrogen from other eutrophic surface waters (e.g., livestock wastewater).

3.5. Potential and sustainability of RCMBA for heavy metal adsorption

The removal effect of recovered RCMBA on Pb^{2+}, Zn^{2+} and Cu^{2+} in the solution are shown in Fig. 12. Fig. 12 showed that RCMBA had a particular adsorption effect on Pb^{2+}, Zn^{2+} and Cu^{2+}, and its removal rates were 98.83%, 92.71% and 94.78%, respectively. It may be because struvite crystallization loaded on the surface of RCMBA produced phosphate ions under the experimental conditions, and the resulting phosphate ions reacted with Pb^{2+}, Zn^{2+} and Cu^{2+} to form precipitation with low solubility (Li et al., 2016c, 2022a, 2022b; Zhu et al., 2022). The adsorption equilibrium capacities of RCMBA were 494.13 mg/g Pb^{2+}, 139.06 mg/g Zn^{2+} and 142.17 mg/g Cu^{2+}, respectively. However, the adsorption performance of recovered RCMBA on heavy metal in the solution needs further study. Future work will focus on the resource utilization of RCMBA.

It should be noted that the BA used in this study is energy solid waste, so the application cost of 400CMBA is much lower than that of conventional adsorbents. In addition, the abundant seawater resources contain a large amount of readily available $MgCl_2$, which can be used for BA residue for modification treatment. Most importantly, 400CMBA consists of BA residue and MgO, both of which are environmentally benign. Compared to conventional adsorbents, 400CMBA enriched with struvite crystallization after adsorption of phosphate and ammonia nitrogen can not only be used as agricultural fertilizer but also as a kind of heavy metal adsorbent. Li et al. (2016b) applied the recovered phosphorus-loaded 20MMSB as a slow-release fertilizer. They significantly increased the ryegrass yield and confirmed the potential of phosphorus-loaded 20MMSB to replace phosphorus-based fertilizers. Thus, using seawater and BA as raw materials for the preparation of 400CMBA for the treatment of phosphate and ammonia nitrogen in water has significant environmental, social, and economic benefits.

4. Conclusion

In this study, a composite material CMBA was developed by in situ-precipitation modification method using the solid waste of energy industry-BA as raw material for the first time. Phosphate and ammonia nitrogen in the sewage sludge supernatant were effectively removed by simple adsorption. Experimental results showed that magnesium oxide could be effectively loaded on the surface of BA at an Mg^{2+} concentration of 1.25 M and a calcination temperature of 400 °C. 400CMBA showed strong adsorption capacity in a wide initial pH value range (at around 5–9), because it has alkalinity self-sufficiency. In addition, the existence of cations or anions in the solution affected the removal of phosphate and ammonia nitrogen to varying degrees. Kinetics and isotherm analysis showed that the removal of phosphate and ammonia nitrogen was controlled by chemisorption and influenced by several adsorption mechanisms at the same time. Thermodynamic parameters indicated that the adsorption process was exothermic and spontaneous. The increase of temperature was not conducive to the removal of phosphate and ammonia nitrogen. CMBA regeneration studies showed that the removal rates of phosphate and ammonia nitrogen were less than 50% and 25%, respectively, at the fifth cycle. Adsorption mechanism analysis showed that the adsorption mechanisms of 400CMBA for phosphate and ammonia nitrogen were mainly physical adsorption, electrostatic attraction, ion exchange, complexation reaction and chemical precipitation, in which chemical precipitation dominated by struvite crystallization was dominant. Furthermore, the removal of BA for ammonia nitrogen by ion exchange could not be ignored. In addition to phosphate and ammonia nitrogen, 400CMBA also showed great removal performance for dissolved organic matter when treating actual sewage sludge supernatants. In addition, the RCMBA showed a special adsorption capacity for Pb^{2+}, Zn^{2+} and Cu^{2+} in the solution. The content of this part needs further study. In conclusion, MgO modification technology could realize the resource utilization of BA from thermal power plant, and simultaneously remove and collect phosphate, ammonia nitrogen and organic matter in sewage sludge supernatants. The RCMBA was not only a potential agricultural fertilizer, but also a heavy metal adsorbent. Overall, this work provides a feasible way for the resource utilization of energy solid waste-BA from thermal power plant, which will promote the industrial solid waste treatment, nutrient recycling, and environmental sustainability.

Declaration of Competing Interest

The authors declare that they have no known competing financial interests or personal relationships that could have appeared to influence the work reported in this paper.

Acknowledgments

This work was supported by the National Natural Science Foundation of China (No. 41672247), "Rejuvenating Liaoning Talents" youth top talent program of Liaoning Province (No. XLYC1807159), discipline innovation team of Liaoning University of engineering and Technology (No. LNTU20TD-21) and Liaoning Provincial Department of Education Project (No. LJKZ0324).

Availability of date and materials

The datasets used or analyzed during the current study are available from the corresponding author on reasonable request.

Appendix A. Supplementary material

Supplementary material to this article can be found online at https://doi.org/10.1016/j.arabjc.2023.104945.

References

Ahmed, S., Rehman, H.U., Ali, Z., Qadeer, A., Haseeb, A., Ajmal, Z., 2021. Solvent assisted synthesis of hierarchical magnesium oxide flowers for adsorption of phosphate and methyl orange: Kinetic,

isotherm, thermodynamic and removal mechanism. Surf. Interfaces 23,. https://doi.org/10.1016/j.surfin.2021.100953 100953.

Albadarin, A.B., Mangwandi, C., Al-Muhtaseb, A.H., Walker, G.M., Allen, S.J., Ahmad, M.N.M., 2012. Kinetic and thermodynamics of chromium ions adsorption onto low-cost dolomite adsorbent. Chem. Eng. J. 179, 193–202. https://doi.org/10.1016/j.cej.2011.10.080.

Amirbahman, A., Lake, B.A., 2013. Seasonal phosphorus dynamics in the surficial sediment of two shallow temperate lakes: a solid-phase and pore-water study. Hydrobiologia 701 (1), 65–77. https://doi.org/10.1007/s10750-012-1257-z.

Bacelo, H., Pintor, A.M.A., Santos, S.C.R., Boaventura, R.A.R., Botelho, C.M.S., 2020. Performance and prospects of different adsorbents for phosphorus uptake and recovery from water. Chem. Eng. J. 381,. https://doi.org/10.1016/j.cej.2019.122566 122566.

Barbosa, R., Lapa, N., Lopes, H., Morujo, A., Mendes, B., 2013. Removal of phosphorus from wastewaters by biomass ashes. Water Sci. Technol. 68 (9), 2019–2027. https://doi.org/10.2166/wst.2013.455.

Bhatnagar, A., Vilar, V.J.P., Botelho, C.M.S., Boaventura, R.A.R., 2011. A review of the use of red mud as adsorbent for the removal of toxic pollutants from water and wastewater. Environ. Technol. 32 (3), 231–249. https://doi.org/10.1080/09593330.2011.560615.

Cavalcante, E.H.M., Candido, I.C.M., Oliveira, H.P., Silveira, K.B., Alvares, T.V.S., Lima, E.C., Mikael, T., Larsson, S.H., Reis, G.S., 2022. 3-Aminopropyl-triethoxysilane-Functionalized Tannin-Rich Grape Biomass for the Adsorption of Methyl Orange Dye: Synthesis, Characterization, and the Adsorption Mechanism. ACS Omega 7 (22), 18997–19009. https://doi.org/10.1021/acsomega.2c02101.

Cheng, X.J., Wang, X.J., Wang, H., Zhang, Z.H., Zhao, J.F., 2017. Simultaneous Recovery of Nutrients from Wastewater by Mesoporous MgO-loaded Natural Zeolital. Environ. Sci. 38 (12), 5339–15145. https://doi.org/10.13227/j.hjkx.201704091.

Cimirro, N.F.G.M., Lima, E.C., Cunha, M.R., Thue, P.S., Grimm, A., Reis, G.S., Rabiee, N., Saeb, M.R., Keivanimehr, F., Habibzadeh, S., 2022. Removal of diphenols using pine biochar. Kinetics, equilibrium, thermodynamics, and mechanism of uptake. J. Mol. Liq. 364,. https://doi.org/10.1016/j.molliq.2022.119979 119979.

Conley, D.J., Paerl, H.W., Howarth, R.W., Boesch, D.F., Seitzinger, S.P., Havens, K.E., Lancelot, C., Likens, G.E., 2009. Ecology controlling eutrophication: nitrogen and phosphorus. Science 323 (5917), 1014–1015. https://doi.org/10.1126/science.1167755.

Di, J.Z., Ruan, Z., Zhang, S.Y., Dong, Y.R., Fu, S.O., Li, H.Z., Jiang, G.L., 2022. Adsorption behaviors and mechanisms of Cu^{2+}, Zn^{2+} and Pb^{2+} by magnetically modified lignite. Sci. Rep. 12 (1), 1394. https://doi.org/10.1038/s41598-022-05453-y.

Dithmer, L., Lipton, A.S., Reitzel, K., Warner, T.E., Lundberg, D., Nielsen, U.G., 2015. Characterization of phosphate sequestration by a lanthanum modified bentonite clay: a solid-state NMR, EXAFS, and PXRD study. Environ. Sci. Tech. 49 (7), 4559–4566. https://doi.org/10.1021/es506182s.

Doyle, J.D., Parsons, S.A., 2002. Struvite formation, control and recovery. Water Res. 36 (16), 3925–3940. https://doi.org/10.1016/S0043-1354(02)00126-4.

Du, X.L., Han, Q., Li, J.Q., Li, H.Y., 2017. The behavior of phosphate adsorption and its reactions on the surfaces of Fe-Mn oxide adsorbent. J. Taiwan Inst. Chem. Eng. 76, 167–175. https://doi.org/10.1016/j.jtice.2017.04.023.

Edet, U.A., Ifelebuegu, A.O., 2020. Kinetics, Isotherms, and Thermodynamic Modeling of the Adsorption of Phosphates from Model Wastewater Using Recycled Brick Waste. Processes 8 (6), 665. https://doi.org/10.3390/pr8060665.

Fan, T.Y., Wang, M., Wang, X.M., Chen, Y.X., Wang, S., Zhan, H. B., Chen, X.Y., Lu, A., Zha, S.J., 2021. Experimental study of the adsorption of nitrogen and phosphorus by natural clay minerals. Adsorpt. Sci. Technol. 2021, 4158151. https://doi.org/10.1155/2021/4158151.

Fan, L.Q., Zhou, X., Liu, Q., Wan, Y., Cai, J., Chen, W., Chen, F.H., Ji, L., Cheng, L., Luo, H.B., 2019. Properties of Eupatorium adenophora Spreng (Crofton Weed) Biochar Produced at Different Pyrolysis Temperatures. Environ. Eng. Sci. 36 (8), 937–946. https://doi.org/10.1089/ees.2019.0028.

Feng, Q.W., Chen, M., Wu, P., Zhang, X.Y., Wang, S.S., Yu, Z.B., Wang, B., 2021. Simultaneous reclaiming phosphate and ammonium from aqueous solutions by calcium alginate-biochar composite: Sorption performance and governing mechanisms. Chem. Eng. J. 429,. https://doi.org/10.1016/j.cej.2021.132166 132166.

Feng, G.R., Ma, J.C., Zhang, X.P., Zhang, Q.F., Xiao, Y.Q., Ma, Q. L., Wang, S.B., 2018. Magnetic natural composite Fe_3O_4-chitosan@bentonite for removal of heavy metals from acid mine drainage. J. Colloid Interface Sci. 538, 132–141. https://doi.org/10.1016/j.jcis.2018.11.087.

González-Hourcade, M., Reis, G.S., Grimm, A., Dinh, V.M., Lima, E. C., Larsson, S.H., Gentili, F.G., 2022. Microalgae biomass as a sustainable precursor to produce nitrogen-doped biochar for efficient removal of emerging pollutants from aqueous media. J. Clean. Prod. 348,. https://doi.org/10.1016/j.jclepro.2022.131280 131280.

Guy, M., Mathieu, M., Anastopoulos, I.P., Martínez, M.G., Rousseau, F., Dotto, G.L., Oliveira, H.P., Lima, E.C., Thyrel, M., Larsson, S.H., Reis, G.S., 2022. Process Parameters Optimization, Characterization, and Application of KOH-Activated Norway Spruce Bark Graphitic Biochars for Efficient Azo Dye Adsorption. Molecules 27 (2), 456. https://doi.org/10.3390/molecules27020456.

Hanhoun, M., Montastruc, L., Azzaro-Pantel, C., Biscans, B., Freche, M., Pibouleau, L., 2011. Temperature impact assessment on struvite solubility product: A thermodynamic modeling approach. Chem. Eng. J. 167 (1), 50–58. https://doi.org/10.1016/j.cej.2010.12.001.

He, Q.S., Li, X.F., Ren, Y.P., 2022. Analysis of the simultaneous adsorption mechanism of ammonium and phosphate on magnesium-modified biochar and the slow release effect of fertilizer. Biochar. 4 (1), 25. https://doi.org/10.1007/s42773-022-00150-5.

Huang, H.M., Zhang, D.D., Wang, W.J., Li, B., Zhao, N., Li, J., Dai, J.K., 2019. Alleviating Na^+ effect on phosphate and potassium recovery from synthetic urine by K-struvite crystallization using different magnesium sources. Sci. Total Environ. 655, 211–219. https://doi.org/10.1016/j.scitotenv.2018.11.259.

Huo, H.X., Lin, H., Dong, Y.B., Cheng, H., Wang, H., Cao, L.X., 2012. Ammonia-nitrogen and phosphates sorption from simulated reclaimed waters by modified clinoptilolite. J. Hazard. Mater. 229, 292–297. https://doi.org/10.1016/j.jhazmat.2012.06.001.

Isik, Z., Saleh, M., Dizge, N., 2021. Adsorption studies of ammonia and phosphate ions onto calcium alginate beads. Surf. Interfaces 26,. https://doi.org/10.1016/j.surfin.2021.101330 101330.

Jiang, Y.H., Li, A.Y., Deng, H., Ye, C.H., Wu, Y.Q., Linmu, Y.D., Hang, H.L., 2018. Characteristics of nitrogen and phosphorus adsorption by Mg-loaded biochar from different feedstocks. Bioresour. Technol. 276, 183–189. https://doi.org/10.1016/j.biortech.2018.12.079.

Kadirova, Z.C., Hojamberdiev, M., Okada, K., 2014. Ion uptake properties of low-cost inorganic sorption materials in the CaO–Al_2O_3–SiO_2 system prepared from phosphogypsum and kaolin. J. Clean. Prod. 83, 483–490. https://doi.org/10.1016/j.jclepro.2014.06.084.

Koh, K.Y., Zhang, S., Chen, J.P., 2019. Hydrothermally synthesized lanthanum carbonate nanorod for adsorption of phosphorus: Material synthesis and optimization, and demonstration of excellent performance. Chem. Eng. J. 380,. https://doi.org/10.1016/j.cej.2019.122153 122153.

Li, A.Y., Ge, W.Z., Liu, L.H., Qiu, G.H., 2022a. Preparation, adsorption performance and mechanism of MgO-loaded biochar in wastewater treatment: A review. Environ. Res. 212,. https://doi.org/10.1016/j.envres.2022.113341 113341.

Li, Z.X., Guo, M.X., Sun, X.W., Li, L.C., Guo, X.L., Huang, L.D., Xiao, J.T., Xu, D.F., Liu, D.G., 2020. High concentration phosphate removal by calcite and its subsequent utilization for tetracycline removal. J. Water Process Eng. 37,. https://doi.org/10.1016/j.jwpe.2020.101412 101412.

Li, Z.W., Huang, B., Huang, J.Q., Chen, G.Q., Xiong, W.P., Nie, X. D., Ma, W.M., Zeng, G.M., 2016c. Influence of different phosphates on adsorption and leaching of Cu and Zn in red soil. Trans. Nonferrous Met. Soc. Chin. 26, 536–543. https://doi.org/10.1016/S1003-6326(16)64142-0.

Li, H.H., Li, X.K., Ding, J.W., Li, X., Zhao, W.T., Liu, M.X., Yu, W. L., 2021. Hierarchical nano-porous biochar prepared by a MgO template method for high performance of PNP adsorption. New J. Chem. 45 (16), 7332–7343. https://doi.org/10.1039/d1nj00157d.

Li, H., Li, H., Jiang, Q., Zhang, J.X., Wang, Y.F., Zhang, Y., 2022b. Synchronization adsorption of Pb(II) and Ce(III) by biochar supported phosphate-doped ferrihydrite in aqueous solution: Adsorption efficiency and mechanisms. Colloids Surf. A Physicochem. Eng. Asp. 648,. https://doi.org/10.1016/j.colsurfa.2022.129230 129230.

Li, R.H., Wang, J.J., Zhou, B.Y., Awasthi, M.K., Ali, A., Zhang, Z. Q., Gaston, L.A., Lahori, A.H., Mahar, A., 2016a. Enhancing phosphate adsorption by Mg/Al layered double hydroxide functionalized biochar with different Mg/Al ratios. Sci. Total Environ. 559, 121–129. https://doi.org/10.1016/j.scitotenv.2016.03.151.

Li, R.H., Wang, J.J., Zhou, B.Y., Awasthi, M.K., Ali, A., Zhang, Z. Q., Lahori, A.H., Mahar, A., 2016b. Recovery of phosphate from aqueous solution by magnesium oxide decorated magnetic biochar and its potential as phosphate-based fertilizer substitute. Bioresour. Technol. 215, 209–214. https://doi.org/10.1016/j.biortech.2016.02.125.

Li, R.H., Wang, J.J., Zhou, B.Y., Zhang, Z.Q., Liu, S., Lei, S., Xiao, R., 2017. Simultaneous capture removal of phosphate, ammonium and organic substances by MgO impregnated biochar and its potential use in swine wastewater treatment. J. Clean. Prod. 147, 96–107. https://doi.org/10.1016/j.jclepro.2017.01.069.

Li, J., Wang, X.J., Wang, J., Li, Y., Xia, S.Q., Zhao, J.F., 2019. Simultaneous recovery of microalgae, ammonium and phosphate from simulated wastewater by MgO modified diatomite. Chem. Eng. J. 362, 802–811. https://doi.org/10.1016/j.cej.2019.01.094.

Lima, A., Nascimento, R.F., Sousa, F.F., Filho, J.M., Oliveira, A.C., 2012. Modified coconut shell fibers: a green and economical sorbent for the removal of anions from aqueous solutions. Chem. Eng. J. 185, 274–284. https://doi.org/10.1016/j.cej.2012.01.037.

Liu, T., Ma, P.C., Yu, J.K., Li, L., Liu, X.M., Ma, B.Y., 2010. Preparation of MgO by thermal decomposition of $Mg(OH)_2$. J. Chin. Ceram. Soc. 38 (7), 1337–1340. https://doi.org/10.14062/j.issn.0454-5648.2010.07.008.

Liu, X.N., Wen, G.Q., Hu, Z.Y., Wang, J., 2018. Coupling effects of pH and Mg/P ratio on P recovery from anaerobic digester supernatant by struvite formation. J. Clean. Prod. 198, 633–641. https://doi.org/10.1016/j.jclepro.2018.07.073.

Lu, J.B., Liu, H.J., Zhao, X., Jefferson, W., Cheng, F., Qu, J.H., 2014. Phosphate removal from water using freshly formed Fe-Mn binary oxide: Adsorption behaviors and mechanisms. Colloids Surf. A Physicochem. Eng. Asp. 455, 11–18. https://doi.org/10.1016/j.colsurfa.2014.04.034.

Lv, N., Li, X.F., Qi, X.G., Ren, Y.P., 2022. Calcium-modified granular attapulgite removed phosphorus from synthetic wastewater containing low-strength phosphorus. Chemosphere 296,. https://doi.org/10.1016/j.chemosphere.2022.133898 133898.

Nguyen, T., Ngo, H.H., Guo, W.S., Zhang, J., Liang, S., Lee, D.J., Nguyen, P.D., Bui, X.T., 2014. Modification of agricultural waste/by-products for enhanced phosphate removal and recovery: potential and obstacles. Bioresour. Technol. 169, 750–762. https://doi.org/10.1016/j.biortech.2014.07.047.

Oginni, O., Yakaboylu, G.A., Singh, K., Sabolsky, E.M., Unal-Tosun, G., Jaisi, D., Khanal, S., Shah, A., 2020. Phosphorus adsorption behaviors of MgO modified biochars derived from waste woody biomass resources. J. Environ. Chem. Eng. 8, (2). https://doi.org/10.1016/j.jece.2020.103723 103723.

Park, N., Chang, H., Jang, Y., Lim, H., Jung, J., Kim, W., 2021. Prediction of adequate pH and Mg^{2+} dosage using an empirical MgO solubility model for struvite crystallization. Environ. Technol. Innov. 21,. https://doi.org/10.1016/j.eti.2020.101347 101347.

Pei, G.F., Wang, Q., Liu, G.X., 2015. The role of periphyton in phosphorus retention in shallow lakes with different trophic status, China. Aquatic Bot. 125, 17–22. https://doi.org/10.1016/j.aquabot.2015.04.005.

Sakthivel, A., Thangagiri, B., Jeyasubramanian, K., Raja, J.D., Krishnamurthy, N., 2021. Switching the hydrophobic Neyveli lignite into hydrophilic type by surface modifcation and its subsequent use for removing Cr(VI)/F—from artifcial pollutant. Fuel 298,. https://doi.org/10.1016/j.fuel.2021.120787 120787.

Salomón, Y.L.O., Georgin, J., Reis, G.S., Lima, É.C., Oliveira, M.L. S., Franco, D.S.P., Netto, M.S., Allasia, D., Dotto, G.L., 2020. Utilization of Pacara Earpod tree (Enterolobium contortisilquum) and Ironwood (Caesalpinia leiostachya) seeds as low-cost biosorbent for removal of basic fuchsin. Environ. Sci. Pollut. Res. 27 (26), 33307–33320. https://doi.org/10.1007/s11356-020-09471-z.

Shirazinezhad, M., Faghihinezhad, M., Baghdadi, M., Ghanbari, M., 2021. Phosphate removal from municipal effluent by a porous MgO-expanded graphite composite as a novel adsorbent: Evaluation of seawater as a natural source of magnesium ions. J. Water Process Eng. 43,. https://doi.org/10.1016/j.jwpe.2021.102232 102232.

Sun, Z.M., Qu, X.S., Wang, G.F., Zheng, S.L., Frost, R.L., 2015. Removal characteristics of ammonium nitrogen from wastewater by modified Ca-bentonites. Appl. Clay Sci. 107, 46–51. https://doi.org/10.1016/j.clay.2015.02.003.

Venkateswarlu, S., Yoon, M., Kim, M.J., 2022. An environmentally benign synthesis of Fe_3O_4 nanoparticles to Fe_3O_4 nanoclusters: rapid separation and removal of Hg(II) from an aqueous medium. Chemosphere 286,. https://doi.org/10.1016/j.chemosphere.2021.131673 131673.

Xiao, L.P., Li, Y., Kong, Q.P., Lan, Y.L., 2021. From wastes to functions: preparation of layered double hydroxides from industrial waste and its removal performance towards phosphates. Environ. Sci. Pollut. Res. 29 (8), 11893–11906. https://doi.org/10.1007/s11356-021-16563-x.

Xie, F.Z., Wu, F.C., Liu, G.J., Mu, Y.S., Feng, C.L., Wang, H.H., Giesy, J.P., 2014. Removal of Phosphate from Eutrophic Lakes through Adsorption by in Situ Formation of Magnesium Hydroxide from Diatomite. Environ. Sci. Tech. 48 (1), 582–590. https://doi.org/10.1021/es4037379.

Xie, F.Z., Song, K., Geng, S.X., Li, L., 2021. Phosphate sequestration and recovery from eutrophication water by in situ magnesium phosphate formation. Water Supply 20 (6), 2226–2236. https://doi.org/10.2166/ws.2020.123.

Xiong, W.P., Tong, J., Yang, Z.H., Zeng, G.M., Zhou, Y.Y., Wang, D.B., Song, P.P., Xu, R., Zhang, C., Cheng, M., 2017. Adsorption of phosphate from aqueous solution using iron-zirconium modified activated carbon nanofiber: Performance and mechanism. J. Colloid Interface Sci. 493, 17–23. https://doi.org/10.1016/j.jcis.2017.01.024.

Xu, L., Cui, H.B., Zheng, X.B., Liang, J.N., Xing, X.Y., Yao, L.G., Chen, Z.J., Zhou, J., 2016. Adsorption of Cu^{2+} in water by biomass ash. Environ. Chem. 35 (8), 1642–1648. https://doi.org/10.2166/wst.2018.095.

Xu, Q.Y., Li, W.P., Ma, L., Cao, D., Owens, G., Chen, Z.L., 2020a. Simultaneous removal of ammonia and phosphate using green synthesized iron oxide nanoparticles dispersed onto zeolite. Sci. Total Environ. 703,. https://doi.org/10.1016/j.scitotenv.2019.135002 135002.

Xu, Z.H., Yuan, Z.H., Zhang, D.F., Chen, W.F., Huang, Y.X., Zhang, T.Q., Tian, D.Q., Deng, H.X., Zhou, Y.W., Sun, Z.H.,

2018. Highly mesoporous activated carbon synthesized by pyrolysis of waste polyester textiles and $MgCl_2$: Physiochemical characteristics and pore-forming mechanism. J. Clean. Prod. 192, 453–461. https://doi.org/10.1016/j.jclepro.2018.05.007.

Xu, W.S., Zheng, W.J., Wang, F.J., Xiong, Q.Z., Shi, X.L., Kalkhajeh, Y.K., Xu, G., Gao, H.J., 2020b. Using iron ion-loaded aminated polyacrylonitrile fiber to efficiently remove wastewater phosphate. Chem. Eng. J. 403,. https://doi.org/10.1016/j.cej.2020.126349 126349.

Yin, Q.Q., Liu, M.T., Ren, H.P., 2019. Biochar produced from the co-pyrolysis of sewage sludge and walnut shell for ammonium and phosphate adsorption from water. J. Environ. Manage. 249,. https://doi.org/10.1016/j.jenvman.2019.109410 109410.

Younes, H., Mahanna, H., El-Etriby, H.K., 2020. Fast adsorption of phosphate (PO_4^-) from wastewater using glauconite. Water Sci. Technol. 80 (9), 1643–1653. https://doi.org/10.2166/wst.2019.410.

Yu, C.A., Jiang, S.Q., Zhang, Y.A., Xu, J., Qiu, L.W., Wang, L.P., 2021. Investigation into adsorption characteristics and mechanism of atrazine on nano-MgO modified fallen leaf biochar. J. Environ. Chem. Eng. 9, 105727. https://doi.org/10.1016/j.jece.2021.105727.

Yu, J., Li, X.D., Wu, M., Lin, K., Xu, L.H., Zeng, T., Shi, H.X., Zhang, M., 2022. Synergistic role of inherent calcium and iron minerals in paper mill sludge biochar for phosphate adsorption. Sci. Total Environ. 834,. https://doi.org/10.1016/j.scitotenv.2022.155193 155193.

Yuan, Y., Zhan, W.Q., Jia, F.F., Song, S.X., 2020. Multi-edged molybdenite achieved by thermal modification for enhancing Pb(II) adsorption in aqueous solutions. Chemosphere 251,. https://doi.org/10.1016/j.chemosphere.2020.126369 126369.

Zeng, W.S., Wang, D.H., Luo, Z.F., Yang, J., Wu, Z.Y., 2020. Phosphorus recovery from pig farm biogas slurry by the catalytic ozonation process with MgO as the catalyst and magnesium source. J. Clean. Prod. 269,. https://doi.org/10.1016/j.jclepro.2020.122133 122133.

Zhang, G.S., Liu, H.J., Liu, R.P., Qu, J.H., 2009. Removal of phosphate from water by a Fe-Mn binary oxide adsorbent. J. Colloid Interface Sci. 335 (2), 168–174. https://doi.org/10.1016/j.jcis.2009.03.019.

Zhang, G.S., Ren, Z.M., Zhang, X.W., Chen, J., 2013. Nanostructured iron(III)-copper(II) binary oxide: A novel adsorbent for enhanced arsenic removal from aqueous solutions. Water Res. 47 (12), 4022–4031. https://doi.org/10.1016/j.watres.2012.11.059.

Zhou, Z.Q. et al, 2012. The development situation of biomass gasification power generation in China. Energy Policy 51, 52–57. https://doi.org/10.1016/j.enpol.2012.05.085.

Zhu, D.C., Chen, Y.Q., Yang, H.P., Wang, S.H., Wang, X.H., Zhang, S.H., Chen, H.P., 2020. Synthesis and characterization of magnesium oxide nanoparticle-containing biochar composites for efficient phosphorus removal from aqueous solution. Chemosphere 247,. https://doi.org/10.1016/j.chemosphere.2020.125847 125847.

Zhu, Z.Q., Wu, Y.Q., Hu, C.Z., Zhang, L.H., Ding, H., Zhu, Y.N., Fan, Y.M., Deng, H., Zhou, X.B., Tang, S., 2022. Elimination of zinc ions from aqueous solution by a hydroxylapatite-biochar composite material with the hierarchical porous microstructures of sugarcane waste. J. Clean. Prod. 362,. https://doi.org/10.1016/j.jclepro.2022.132483 132483.

Zin, M., Kim, D.J., 2020. Simultaneous recovery of phosphorus and nitrogen from sewage sludge ash and food wastewater as struvite by Mg-biochar. J. Hazard. Mater. 403,. https://doi.org/10.1016/j.jhazmat.2020.123704 123704.